Field, textural, geochemical, and isotopic constraints on the origin and evolution of the magmatic microgranular enclaves from the Gharib Granitoid Complex, North Eastern Desert, Egypt

H.A. Eliwa [a,*], R. Deevsalar [b], N.M. Mahdy [c], S. Kumar [d], Kh. El-Gameel [a], T. Zafar [e], I.M. Khalaf [a], M. Murata [f], H. Ozawa [f], A. Andresen [g], D. Chew [h], M.M. Fawzy [c], A. Afandy [c], Y. Kato [i], K. Fujinaga [i]

[a] Geology Department, Faculty of Science, Menoufia University, Shebin El Kom, Egypt
[b] Department of Physics and Earth Science, University of the Ryukyus, Okinawa 903-0213, Japan
[c] Nuclear Materials Authority, P.O. 530, El-Maadi, Cairo, Egypt
[d] Department of Geology, Kumaun University, Nainital, 263 002, India
[e] State Key Laboratory of Ore Deposit Geochemistry, Institute of Geochemistry, Chinese Academy of Sciences, Guiyang 550081, China
[f] National University of Corporation, Naruto University of Education, Department of Geosciences, Faculty of Science Naruto, Tokushima 772-8502, Japan
[g] Department of Geosciences, University of Oslo, Oslo, Norway
[h] Department of Geology, School of Natural Sciences, Trinity College Dublin, Dublin 2, Ireland
[i] Department of Geosystem Engineering, School of Engineering, The University of Tokyo, 7-3-1, Hongo, Bunkyo, Tokyo 113-8656, Japan

ARTICLE INFO

ABSTRACT

The Neoproterozoic Gharib Granitoid Complex (GGC), in the North Eastern Desert (NED) of Egypt, is characterized by the occurrence of varieties of granitoids. Monzogranite, the most abundant granite variety, contains abundant magmatic microgranular enclaves (MMEs) of mafic to intermediate composition. The MMEs are more mafic than their host and marked by a greater amount of amphibole and biotite. They are finer grained and have porphyritic/poikilitic textures.

The sharp, crenulated, and fine-grained quenched contacts of the elongated, rounded, and ellipsoid form of the MMEs with their felsic host indicate rapid cooling during a magma mixing/mingling event. Micro-textural evidence supports the mechanical transfer of minerals that crystallized in felsic magma to the mafic melt (e.g., feldspar phenocrysts cross-cutting the MME-host boundaries, stubby apatite, quartz ocelli, and poikilitic outermost rims of K-feldspar phenocrysts), supercooling/quenching process (e.g., acicular apatite and elongated hornblende and biotite crystals), and disequilibrium growth (e.g., hornblende-biotite clots replaced early crystallized clinopyroxene), which also favour a magma mingling/mixing origin. Linear to curvilinear chemical variations of the MMEs and the host monzogranites on Harker diagrams, highly similar trace element contents, and Sr-Nd isotopic systematics together with mineral-chemical features also support mixing/mingling as the main process in magma genesis and strongly suggest that the MMEs were supercooled hybrid globules within cooler, partially crystallized host felsic magma. The crust-like geochemical signatures (i.e., SiO_2 content, metaluminous nature, and lack of upper crustal xenoliths and typical peraluminous minerals), along with low [MMEs: $(^{87}Sr/^{86}Sr)_{initial}$ = 0.70136–0.70373; monzogranites: $(^{87}Sr/^{86}Sr)_{initial}$ = 0.70202–0.70320)] along with zircon and apatite U-Pb age data indicate the possible involvement of juvenile lower continental crust (LCC) of the Arabian-Nubian Shield (ANS) in their genesis. The medium- to high-K calc-alkaline affinity, the LILE enrichment, and the HFSE depletion along with low Nb/La ratios and positive $\varepsilon Nd_{(t)}$ (MMEs = +4.01 - +5.62, monzogranites = +2.29 - +6.03) indicate the contribution of depleted lithospheric mantle in the magma genesis, whereas the low δEu and fairly high δCe values, stable La/Sm, and variable Sr/Th ratios in apatites from the monzogranites and MMEs indicate the contribution of volatile/fluids from the remnants of the oceanic slab in facilitating melting in the source region. The genesis of the monzogranites and MMEs started with asthenosphere upwelling, followed by melting of the remnants of lithospheric mantle, and underplating of mantle magma, which led to partial melting of the LCC. Multi-element modelling postulates that the low degree mixing between

* Corresponding author.
E-mail address: eliwa98@hotmail.com (H.A. Eliwa).

partially crystallized mantle magma and LCC-derived felsic melt ($F_{mix} \sim 0.1$) could produce the parent magma for the monzogranites. Further mixing/mingling of the crystal-charged monzogranite parent magma with new pulses of mafic melts ($F_{mix} \sim 0.25$) developed a hybrid zone and formed the hybrid MMEs. Thus, the final episode of the ANS evolution was associated with a complex post-collisional interplay between asthenosphere, lithospheric mantle, and the LCC caused by the removal of delaminated lithospheric root and dense lower crust following the collision between East and West Gondwana in the Neoproterozoic time.

1. Introduction

The Arabian Nubian Shield (ANS) is an important crustal block with a distinct geological architecture that originated and evolved during the Neoproterozoic time. It is comprised of intra-oceanic arc terranes, which are separated by sutures commonly defined by ophiolites. The ANS covers $> 6 \times 10^6$ km^2 including parts of Egypt, Eritrea, Ethiopia, Saudi Arabia, Somalia, Sudan, Oman, Yemen, and Jordan, and represents one of the largest Neoproterozoic crustal growth events on the Earth (e.g., Kusky et al., 2003; Stern et al., 2006; Hargrove et al., 2006). The ANS is an accretionary orogen (850–550 Ma) that occurred in three tectonic stages: intra-ocean ridge subduction and arc magmatism (900–750 Ma), *syn*-collisional events and terrane amalgamation (750–620 Ma), and post-collisional extensional regimes (620–550 Ma) (Kusky et al., 2003; Stern et al., 2006; Avigad and Gvirtzman, 2009; Stern and Johnson, 2010; Johnson et al., 2011; Fritz et al., 2013; Garfunkel, 2015; Stern, 2018).

The Gharib Granitoid Complex (GGC) in the North Eastern Desert (NED) of Egypt (Fig. 1a) was emplaced at the final stage of ANS evolution during post-collisional events. It is characterized by spectacular exposures of calc-alkaline and alkaline/peralkaline granitoid plutons (Abdel-Rahman, 1995; Eliwa et al., 2014, El-Bialy et al., 2020). Some of these granitoids enclose ubiquitous mafic enclaves of different sizes, geometries, and compositions. The occurrence of magmatic microgranular enclaves (MMEs) is a common feature of most calc-alkaline granitoids in the region, especially in the NED and southern Sinai.

In this study, an integrated field-based petrographic, textural, and mineralogical approach along with geochemical and isotopic investigations are applied to unravel the processes responsible for the generation and evolution of the MMEs and host monzogranites in the GGC.

2. Geological setting

The study area (latitudes 27° 50′ to 28° 05′ and longitudes 32° 50′ to 33° 05′) is part of the Ras Gharib crustal block in the NED, Egypt, and herein is referred to as the "Gharib complex". This basement complex exposed in the Eastern Desert and southern Sinai Peninsula together with the isolated inliers in the southern Western Desert of Egypt constitute the north western portion of the ANS (Fig. 1a, b). The Egyptian Eastern Desert has been divided into three distinct basement provinces (Stern and Hedge, 1985), namely; the North Eastern Desert (NED), Central Eastern Desert (CED), and South Eastern Desert (SED). Mafic and intermediate volcanic rocks, greywackes, ophiolitic rocks, gneisses, and migmatites dominate in the CED and SED, whereas granites are abundant in the NED (Fig. 1c). There is strong evidence for
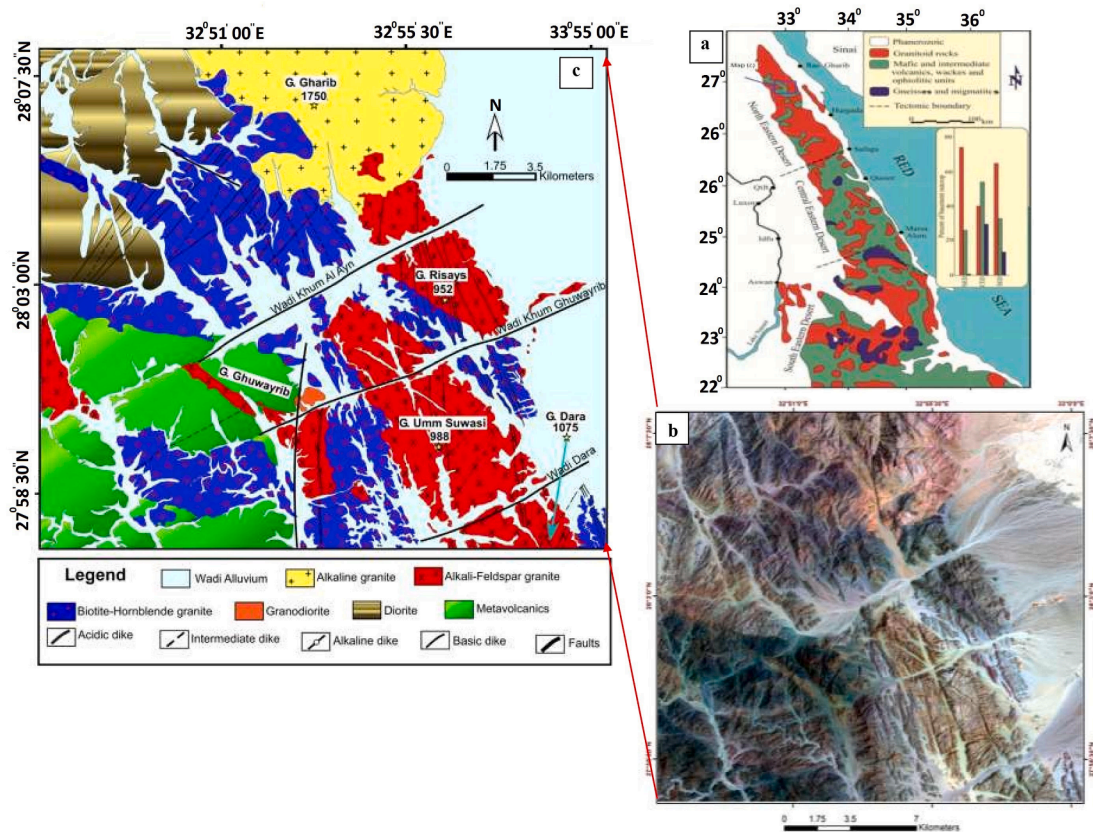
Fig. 1. (**a**) Geological map of the Eastern Desert of Egypt displaying the exposed different rock units, (**b**) Satellite image of the Gharib complex, and (**c**) Geological map of the study area in the Gharib complex, Eastern Desert, Egypt.

extension, in the form of abundant ~600 Ma bimodal dyke swarms trending E-W to NE-SW, indicating ~ N-S extension broadly co-eval with the NW-SW oriented Najd strike-slip deformation in the CED (Stern et al., 1984).

The GGC in the ANS have received considerable attention because of their significant petrological diversities (e.g., Stern and Hedge, 1985; Abdel-Rahman and Martin, 1990; El-Mansi et al., 2004; Eliwa et al., 2014). Based on field relationships, geochemical characteristics, and Rb-Sr whole-rock dating, the magmatic components of the Ras Gharib segment have been divided into six rock suites (Abdel-Rahman, 1995): (1) diorite-tonalite complex (881 ± 58 Ma), (2) the basalt to rhyolite Dokhan Volcanics (620 ± 16 Ma), (3) a composite granodiorite-adamellite-leucogranite batholith (552 ± 7 Ma), (4) trondhjemite pluton (516 ± 7 Ma), (5) dyke swarms (493 ± 7 Ma), and (6) Gharib alkaline granites (476 ± 2 Ma). Eliwa et al. (2014) reported U-Pb SHRIMP zircon ages of 608 ± 3 Ma for a biotite-hornblende (BH) granite and 600 ± 3 Ma for an alkali feldspar (AF) granite, to the south of the study area. Both the monzogranites and the AF granites belong to the granodiorite-adamellite-leucogranite composite batholith of Abdel-Rahman (1995).

3. Field observations and petrography

Field and petrographic observations and regional geological relationships (Stern and Hedge, 1985; Abdel-Rahman and Martin, 1990; Eliwa et al., 2014) show the following magmatic sequence in the Gharib complex: (a) intrusion of quartz diorites and granodiorites, (b) extrusion of the Dokhan Volcanics, (c) emplacement of the monzogranites and alkali feldspar granites (AF), and ending with the (d) intrusion of alkaline granites and dykes (Fig. 1c).

In the present study, we focus on the monzogranites and their MMEs, which occupy most of the mapped study area. The monzogranites crop out as masses of moderate to high relief and of variable size; a big mass to the west of Gabal Gharib and relatively minor masses along the Wadi Khurm Ghuwayrib are observed (Fig. 1c). The monzogranites are pink, (very) coarse-grained rocks with numerous clots of hornblende and biotite and show varying degrees of exfoliation (onion skin) weathering. However, the mineralogical and textural characteristics of the monzogranites are quite similar throughout the region, although locally the content of biotite and hornblende varies considerably from low (<2 vol %) to high (~10 vol%). They frequently contain MMEs, which have a
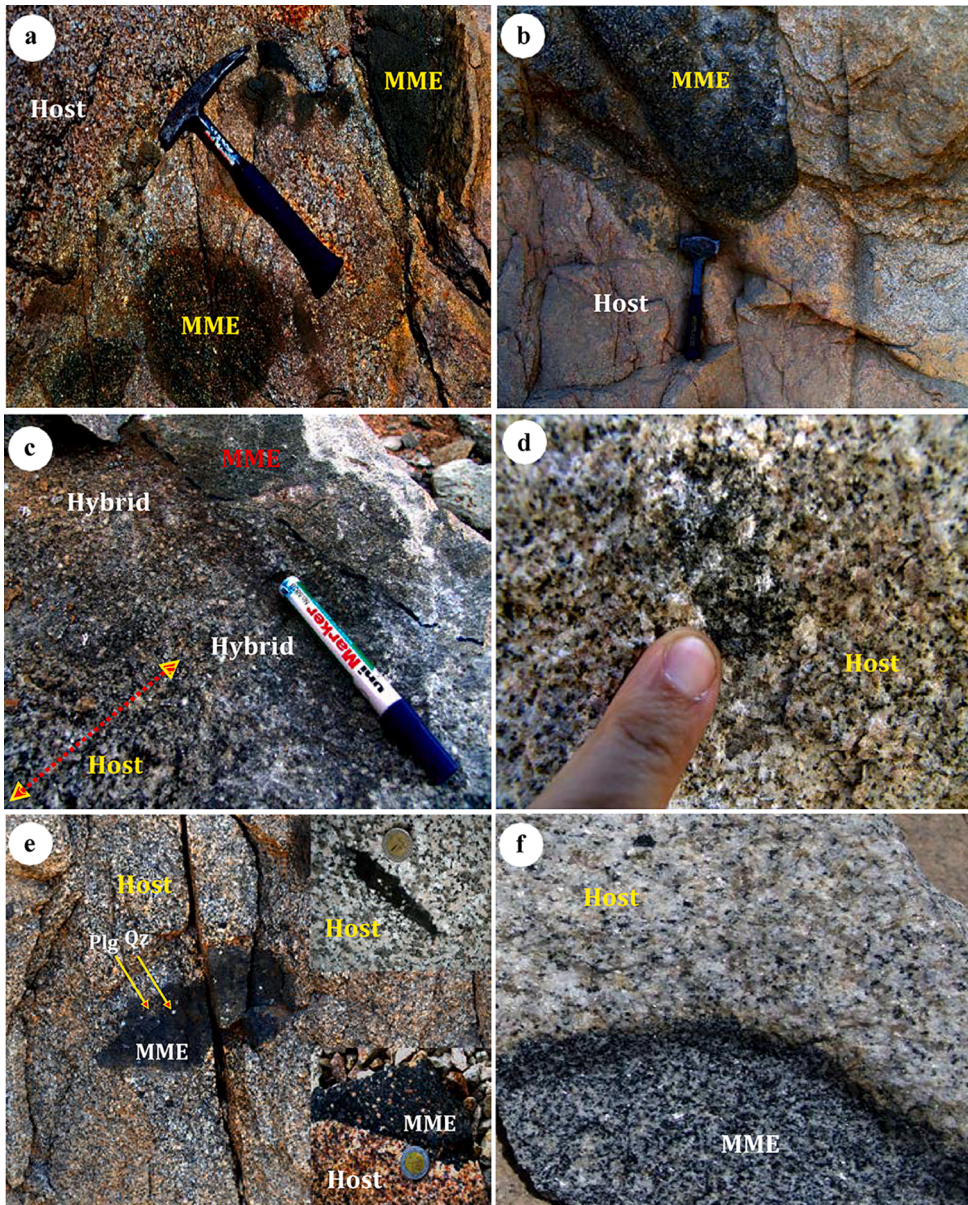
Fig. 2. Field photographs displaying geological features of the enclaves (MMEs); (**a**) Various sizes and shapes of mafic MMEs in the host monzogranite. Arrows point to the MMEs, (**b**) Dark mafic and porphyritic textured MME within the monzogranite exhibiting sharp contact. (**c**) Gradational contact of the host monzogranites with MMEs showing hybrid zone, (**d**) Diffused contact between the MME and host monzogranite, (**e**) Quartz and plagioclase phenocrysts within MMEs. Note to the crenulated to cuspate and sharp contacts and viscous finger structures between MMEs and host. Arrows point to the phenocrysts, (**f**) A dark and mafics-rich continuous contact margin between MMEs and monzogranite, (**g**) Fine-grained chilled margin at contact between MMEs and host monzogranites, (**h**) Fragments of host granite mass (0.5 m) with angular to sub-rounded edges are contained with hybrid-MME rock with sharp contact, (**i**) Numerous *syn*-plutonic dyke swarms are cross-cutting the host monzogranites, (**j**) Alignment of flattened and elongated MMEs showing stretching and deformation within host monzogranites, (**k**) Hybridization zone of a mixture of the MMEs and monzogranites and their complicated relation showing magmatic flow and deformation in the MME as appointed by red arrows, (**l**) Rounded micro-dioritic enclave with viscous finger structure, and (**m**) Pillow-like structured MME.
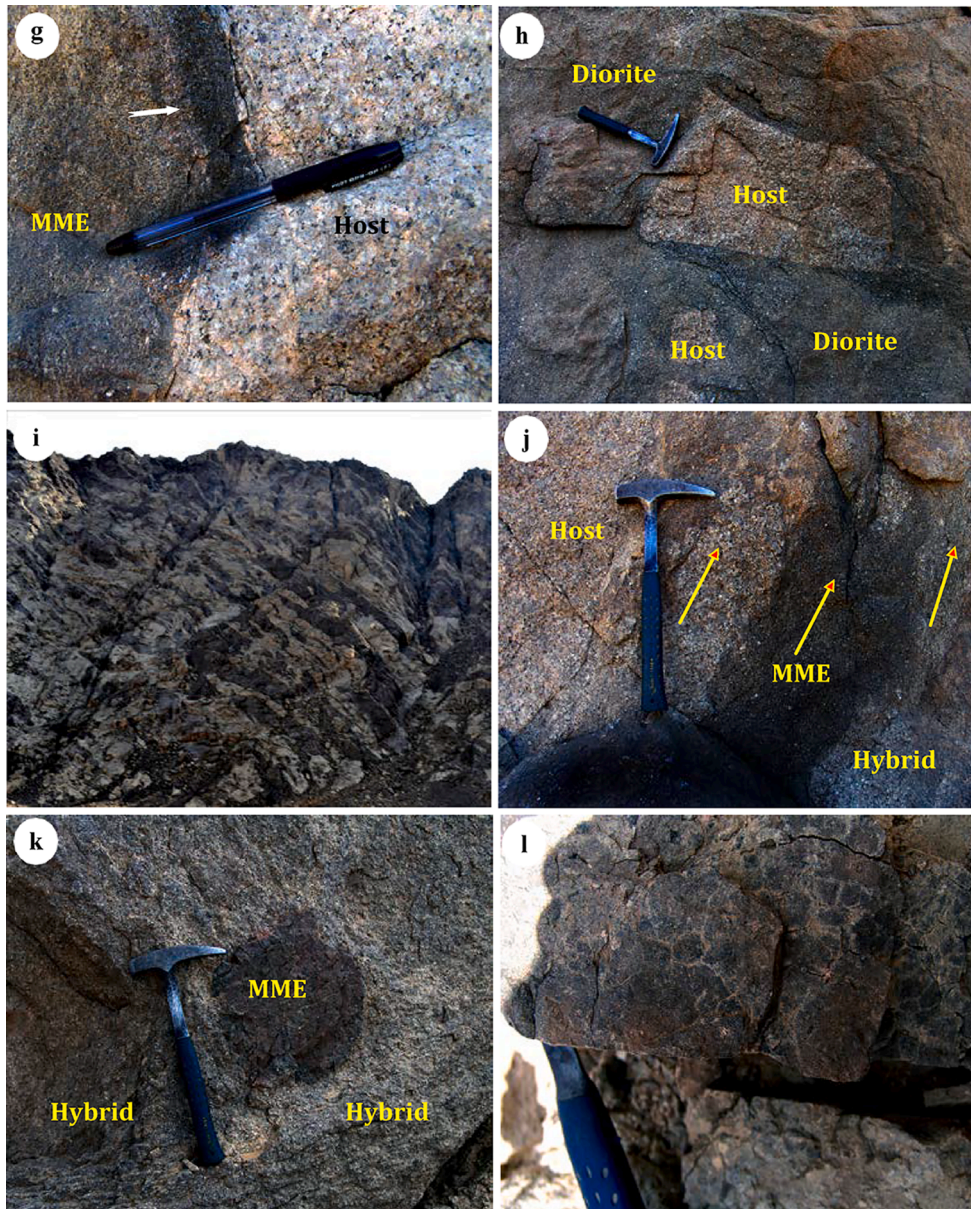
mafic to intermediate composition, porphyritic texture with abundant felsic phenocrysts and sharp contacts with their host (Supplementary Item-I, Fig. S1a). They are crosscut by dykes and dyke swarms of felsic to intermediate (Supplementary Item-I, Fig. S1b), and less rarely mafic compositions. In rare cases, monzogranites occur as dyke-like 'trails', probably representing *syn*-plutonic intrusive bodies intruding the diorites with locally sharp contacts.

The MMEs are widely distributed throughout the entire monzogranite and granodiorite intrusions at their outer marginal parts. They vary from mostly rounded to subrounded, elongated, spheroidal, and ellipsoidal in shape and exhibit a wide variation in their size ranging from a few millimetres to tens of centimetres (up to 1.5 m long). The contacts of the MMEs with the host monzogranites are variable ranging from sharp (Fig. 2a, b), through gradational (Fig. 2c), crenulated or cuspate to diffuse (Fig. 2d). The sharp contacts are common and have regular or irregular outlines, while the gradational contacts are less common and are accompanied by a change in the composition and/or grain-size. Phenocrysts/megacrysts of K-feldspar, plagioclase, and/or quartz, which are often rounded in the MMEs, occur notably within and/ or crosscut the boundaries between the MMEs and the host

monzogranites (Fig. 2e). The MMEs bear the same mineral assemblage as the monzogranites, but with more ferromagnesian minerals, which together with their fine-grained texture render the MMEs darker than their host (Fig. 2f). Ferromagnesian minerals, such as biotite and hornblende are more abundant in the outer rims of most MMEs (Fig. 2f). The fine-grained, porphyritic texture of the MMEs (Fig. 2e) is delineated by abundant phenocrysts/megacrysts and sometimes exhibit a decrease in grain size close to the contacts with host granites resulting in a darker rim representing likely chilled margins (Fig. 2f, g). Rarely thin leucocratic continuous/ discontinuous selvages of mainly quartz and K-feldspar are seen around the MMEs within the monzogranites.

Diffuse, gradational, and irregular contacts and complex intergrowths and intercalations between the MMEs and the host monzogranites marking a zone of interaction (hybridization) between two contrasting magmas can be identified in outcrop (Fig. 2k). The xenolithlike angular to sub-rounded, elongate (up to 0.5 m long), and ellipsoidal fragments of the monzogranites with sharp contacts are occasionally present within intermediate dioritic dykes and dyke swarms (Fig. 2h, i), which likely represent the remnants of the host monzogranites in conduit walls entrained into the dioritic magma. The MMEs often exhibit

a preferred orientation within the monzogranites defined by parallel alignment of flattened, elongated and stretched MMEs, which is commonly attributed to magmatic flow. While some of the MMEs show complex textures and structures suggestive of magmatic flow and dynamic stretching and rotation under the influence of convection currents, the others show magmatic deformation as a result of the forcible injection of this magma into the felsic magma chamber. These MMEs are observed with and without magmatic flow fabrics (Fig. 2j). The evidence for solid-state deformation, including fracturing, jointing, and sharp displacements of the contacts in host rock, has also been found in the MMEs (Fig. 2l). Figure (2m) shows MMEs crosscut by a network of felsic veins associated with back-veining and injection of the host granite resulting in pillow-like structures.

Thirty-six and forty-two samples of MMEs and the host monzogranites were plotted on a QAPF (Streckeisen) diagram. The MMEs exhibit gabbro, monzogabbro to diorite, and quartz diorite compositions, while the host granites are mainly monzogranitic, which is supported by the normative mineral based Q-ANOR classification system (Supplementary Item-I, Fig. S2) of Streckeisen and Le Maitre (1979). Detailed descriptions of mineralogy and texture of the MMEs and monzogranites are represented in Table 1 and shown in Fig. 3.

4. Mineral chemistry

The chemical composition of plagioclase, biotite, and amphibole from the monzogranites and associated MMEs are reported in Tables 1 to 3 and the analytical methods are detailed in Supplementary Item-II, Section 1.

4.1. Plagioclase

Representative plagioclases with the lowest degree of alteration from the MMEs and the monzogranites have been selected for microprobe analysis. The results are given in Supplementary Item-III, Table S1 and illustrated on the An-Ab-Or ternary system (Deer et al., 1966; Fig. 4a). They range in composition from oligoclase to andesine (An_{13-43}) in the MMEs and range from albite to oligoclase (An_{6-30}) in the monzogranites, with an average oligoclase composition in both types (Fig. 4a). The plagioclase An% contents in the MMEs are similar to those in the monzogranites, excluding the more anorthitic plagioclase in sample GRC-22EN (Supplementary Item-III, Table S1). Plagioclase phenocrysts from the MMEs sometimes show an anorthite (An_{47}) spike (Fig. 3b).

4.2. Biotite

Representative analyses and structure formulae of biotite from the MMEs and monzogranites are presented in Supplementary Item-III, Table S2. The relatively low $Fe^{\#}$ ratios ($Fe^{+2}/(Fe^{+2} + Mg^{+2}) > 0.3$) in these rocks indicate a magmatic origin on an annite-siderophyllite-phlogopite-eastonite quadrilateral diagram (Speer, 1984). Based on the FeO^t-TiO_2-MgO ternary diagram (Monier 1985; Nachit et al., 2005), the biotites are of almost primary magmatic type with a few re-equilibrated biotites (Supplementary Item-I, Fig. S4a; Supplementary Item-III, Table S2). On the binary plot of Tischendorf et al. (1997) (Fig. 4b), the biotites are classified as Mg-biotite. The FeO^t/MgO ratios range from 1.0 to 1.5 with an average of 1.3 in the MMEs and range from 1.4 to 1.9 with an average of 1.5 in the monzogranites. These values are close to those of the Mg-biotites typically associated with calcic pyroxene and/or calcic amphibole commonly found in calc-alkaline (mostly orogenic and subduction-related) metaluminous (I-type) granites (Abdel-Rahman, 1994). On the ternary MgO-FeO^t-Al_2O_3 plot (Supplementary Item-I, Fig. S4b), all biotites lie in the field of calc-alkaline orogenic suites, which is consistent with the VAG (I-type granites) on tectonic setting discrimination plots (Supplementary Item-I, Fig. S5a-d). Most importantly, the analyzed biotites lie in the field of a crust-mantle mixed source on the $FeO^t/(FeO^t + MgO)$ *vs* MgO plot of Zhou (1986)

Table 1
Mineralogy and texture of the monzogranites and associated MMEs.

Monzogranites Main minerals	Accessory minerals	Secondary minerals	Texture
Quartz, K-feldspar, plagioclase, biotite, and hornblende	Magnetite, ilmenite, titanite, allanite, zircon, and apatite	Sericite, chlorite, epidote, and kaolinite	medium to coarse-grained, equigranular and hypidiomorphic

Kfs	K-feldspar are prismatic to tabular orthoclase and microcline with frequent exsolved patchy, flame, film, veinlets, and braided lamellae of perthites. Poikilitic feldspars encloses fine-grained main phases plus titanite.
Pl	Plagioclase has oligoclase composition and occurs as subhedral to euhedral platy crystals, which commonly exhibit complex zoning patterns (Supplementary Item-I, Fig. S3a) with albite twinning, and are variably altered to sericite and epidote in few samples. They show subsolidus granophyric and myrmekitic intergrowths.
Qz	Quartz is an interstitial phase with anhedral to subhedral crystals
Bt	Biotite forms fresh subhedral flakes, which are strongly pleochroic, but some are partially altered to chlorite with titanite and magnetite along their cleavage planes.
Hbl	Hornblende occurs as subhedral to euhedral elongated tabular crystals with simple twinning. It is strongly pleochroic with poikilitic inclusions of apatite needles, magnetite, and ilmenite and are closely associated with biotite in some samples (Supplementary Item-I, Fig. S3b).
Aln	Allanite occurs as euhedral prismatic zoned crystals and exhibits faint pleochroism from pale reddish-brown to dark brown.
Mat	Magnetite occurs as individual cryst\als and aggregates, which are commonly associated with ferromagnesian minerals, e.g. hornblende and biotite

MMEs Main minerals	Accessory minerals	Secondary minerals	Texture
Plagioclase (55–80%), amphibole (5–10%), biotite (5–15%), K-feldspar (0–8%), and quartz (1–10%)	Magnetite, ilmenite, titanite, apatite, and zircon.	Sericite, chlorite, and epidote,	fine- to medium-grained equigranular to porphyritic textures

Pl	Plagioclase occurs both as small subhedral laths in the groundmass and as large, euhedral to subhedral, tabular, equant, skeletal, and prismatic phenocrysts (Fig. 3a-c) or megacrysts. The important features developed in plagioclase are: Glomeroporphyritic texture (Fig. 3a); complex growth zoning, partial dissolution (resorption), and cellular, patchy (non-patchy rims) and spongy textures (Fig. 3b-c); anti-rapakivi-like texture, with an outer zone poikilitically sieved by tiny crystals of plagioclase, hornblende, biotite, apatite, magnetite, and ilmenite (Fig. 3d).
Kfs	K-feldspar is present as both interstitial phase and subhedral, equant to tabular phenocrysts. The phenocrysts exhibit exsolved perthites, resorption, and outer rims with fine poikilitic inclusions of plagioclase, biotite, hornblende, and quartz (Fig. 3b-d). They display albite, pericline, and combined Carlsbad-albite twinning.
Qz	Quartz occurs as interstitial grains (Fig. 6k-l), large ocellar (rounded) crystals with epitaxial growths of fine plagioclase, hornblende, and biotite crystals (Fig. 3e), grains with wavy extinction and sharp embayed and engulfed boundaries, and anhedral megacrysts enclosing fine inclusions of plagioclase, apatite and titanite (Fig. 3f).
Hbl*	Hornblende forms subhedral to euhedral prisms which often are skeletal with occasional patchy domains that indicate subsolidus re-equilibration (Fig. 3g-h). Hornblende also occurs as fine prisms in the groundmass. Hornblende phenocrysts are crudely oriented, corroded, engulfed, and sieved by groundmass constituents and show simple twinning (Fig. 3b). They are altered to biotite ± chlorite ± epidote (Fig. 3g-h). The resorption, corrosion and parallel alignment of hornblende and biotite indicate magmatic flow deformation (Fig. 3g).
Bt*	Biotite occurs as variably deformed anhedral flakes altered to chlorite with or without irregular patches of Fe-Ti oxides along the cleavages and grain boundaries, and as subhedral blade-shaped fresh and strongly pleochroic flakes (Fig. 3a-f). Biotite and hornblende together with Fe-Ti oxides and titanite form fine-grained mafic clots, which are intervened and enclosed by feldspar and quartz (Fig. 3i).
Ap	The apatite occurs as acicular (elongated needle-shaped) and stubby prismatic crystals (Fig. 3j-k).

Table 1 (*continued*)

	Monzogranites			
	Main minerals	Accessory minerals	Secondary minerals	Texture
Ttn	Titanite occurs as subhedral interstitial and large wedge-like shaped crystals, often associated with plagioclase, magnetite, ilmenite, and biotite (Fig. 3l).			
* These are present in higher abundances than host monzogranites.				

Table 2

Mineralogy and texture of the GRC-101 and associated MMEs (GRC-101EN), along with physical characteristics of the separated zircon (Zrn) and apatite (Ap).

	GRC-101		
	Main minerals	Accessory minerals	Texture
	Quartz, K-feldspar, plagioclase, biotite, and hornblende	Magnetite, ilmenite, titanite, zircon (zrn), and apatite (ap)	Coarse-grained, equigranular, and hypidiomorphic
	Physical properties of the separated minerals		
Zrn	Separated zircon are almost homogenous, transparent, colourless to yellowish in colour, and subhedral to euhedral prismatic. They exhibit oscillatory zoning and are inclusion-free or enclose fine grains of apatite and opaques. Prismatic zircons have sizes ranging from 150 to 300 μm (length) and 50–130 μm (width) with aspect (L/W) ratios of 2:1 to 3:1.		
Ap	Apatites are transparent, colourless, and stubby to prismatic and occasionally acicular, typically inclusion-free, and are up to 100 μm long with an aspect ratio of about 2.5:1.		
	GRC-101EN		
	Main minerals	Accessory minerals	Texture
	Plagioclase, amphibole, biotite, quartz, and K-feldspar set in a fine-grained groundmass composed of the same mineral assemblage	Magnetite, ilmenite, apatite, titanite, and zircon	Xenomorphic to hypidiomorphic with porphyritic to poikilitic phenocrysts
	Physical properties of the separated minerals		
Zrn	The separated zircon crystals are homogenous, transparent to translucent, colourless to light yellow to brownish in colour, and subhedral prismatic to rarely equant. They show faint oscillatory zoning and contain many inclusions of apatite and opaque phases. The size of most zircons ranges from 80 to 180 μm (length) and 40–80 μm (width) with aspect ratios of 1:1 to 2:1. A few large zircons, which resemble the zircons of the host BH granites in morphology, are present too.		
Ap	The separated apatites are usually transparent to rarely translucent, colourless, and mainly of acicular habit. Most grains are inclusion-free, and long acicular crystals are sometimes broken in segments along their c-axis. The crystals are up to 400 μm long with aspect ratio between 10:1 and 30:1.		

(Supplementary Item-I, Fig. S4c).

The crystallization temperatures of the biotites in the monzogranites and MMEs on a Ti *vs* Mg/(Mg + Fe) diagram of Henry et al. (2005) are 680–713 °C and 678–691 °C, respectively (Supplementary Item-I, Fig. S4d; Supplementary Item-III, Table S2). These are near-solidus average magmatic temperatures and consistent with a water-saturated granodiorite solidus (e.g., Conard et al., 1988).

4.3. Amphibole

The chemical composition and structure formulae of representative amphiboles from the MMEs and monzogranites are given in Supplementary Item-III, Table S3. All amphiboles belong to the calcic amphibole group (Supplementary Item-I, Fig. S6a), and are classified as magnesio-hornblende, except two points in an amphibole rim from a MMEs classified as actinolite using the IMA classification scheme (Leake et al., 1997) (Fig. 4c). The Mg-rich amphiboles display pargasitic and edenitic substitutions (Supplementary Item-I, Fig. S6b), that most likely took place under post-magmatic conditions. Compared to the host monzogranites, amphiboles that crystallized in the MMEs have generally

higher Si, Mg, and Fe^{3+} and lower Fe^{2+}, Ti, and Al contents, although there is some compositional overlap, which indicates formation under the same magmatic conditions.

5. Geochronology

U-Pb zircon and apatite age determinations were undertaken on the monzogranite and their MMEs. The analytical methods are presented in Supplementary Item-II, Section 2, and the results are given in Supplementary Item-III, Table S4-5. The LA-ICP-MS dating typically employed two to three spots on both the margins and centre of the selected grains. Two samples have been selected for geochronology; the GRC-21 sample is a coarse-grained monzogranite and contains 30 cm long MME (GRC-21EN) of granodiorite composition.

The GRC-21EN MME is ellipsoidal in shape and has a crenulated surface and sharp, partly diffused contacts. The border between GRC-21 and GRC-21EN is cross-cut by feldspar phenocrysts. The MME is similar in appearance to its host monzogranite, but is darker in colour due to its higher content of ferromagnesian minerals and finer-grained texture. The petrography of these rocks and the morphology of the separated zircons and apatites are described in Table 2.

The LA-ICP-MS zircon U-Pb isotopic analysis (Supplementary Item-III, Table S4) of the monzogranite (GRC-21) yielded a weighted mean age of 612 ± 10 Ma (MSWD = 6.1), which is considered to be the crystallization age of the monzogranites (Fig. 5a). Two age outliers include a crystal, which yielded an older $^{206}Pb/^{238}U$ age of 731 ± 10 Ma for its core, suggesting an inherited origin and another zircon that yielded a younger $^{206}Pb/^{238}U$ age of 474 ± 6 Ma, interpreted as Pb loss. The small and coarse zircon populations from the GRC-21EN yielded similar ages and a weighted mean age of 617 ± 10 Ma (MSWD = 6.7) (Fig. 5b). Core analyses of two coarse zircon crystals from GRC-21EN yielded $^{206}Pb/^{238}U$ ages of 762 ± 9 and 723 ± 11 Ma respectively, suggesting an inherited origin. Two other zircons yielded anomalously young $^{206}Pb/^{238}U$ ages of 531 ± 14 and 474 ± 6 Ma, respectively, probably caused by Pb loss.

The apatite isotopic data (Supplementary Item-II, Table S5) obtained from the monzogranite (GRC-21) and the granodiorite MME (GRC-21EN) define a Tera-Wasserburg discordia with $^{207}Pb/^{206}Pb$ initial values of 0.8761 and 0.8762 and lower intercept ages of 600 ± 20 Ma (MSWD = 2.4) and 608 ± 19 Ma (MSWD = 2.3), respectively (Fig. 5c, d).

6. Whole rock geochemistry

A total of 30 samples, 18 MMEs and 12 host monzogranites were selected for major and trace elements, and rare earth elements (REE) analyses. The results are listed in Table 3 and the analytical methods are detailed in Supplementary Item-II, Section 3.

The monzogranites are relatively enriched in SiO_2 and K_2O, and depleted in TiO_2, Al_2O_3, FeO^t, MgO, CaO, and P_2O_5 compared to the MMEs (Table 3 and Fig. 6). These variations are consistent with the monzogranites and MMEs mineralogy and the mineral abundances. On Harker variation diagrams (Fig. 6), MgO, TiO_2, Al_2O_3, CaO, P_2O_5, and FeO^t in both the monzogranites and MMEs exhibit continuously negatively correlated linear to curvilinear variation trends against increasing SiO_2 content. Although, Zr, La, Ce, and Y broadly show linear trends, the Rb, Sr, Cr, and to some extent Na_2O and K_2O show wide data scatter against SiO_2.

While the host monzogranites plot primarily within the subalkaline granite field on a total alkali-silica (TAS) diagram of Cox et al., (1979), the MMEs of monzodiorite, quartz diorite, and occasionally gabbro composition are plot close to the subalkaline - alkaline granite boundary (Supplementary Item-I, Fig. S7a). On a K_2O *vs*. SiO_2 plot (Supplementary Item-I, Fig. S7b; Peccerillo and Taylor, 1976), the MMEs are medium to high-K calc-alkaline, and the host monzogranites show high-K calc-alkaline affinities. However, the wide range of $Na_2O + K_2O - CaO$ values for monzogranites (2.74–8.06), and MMEs (-2.98–6.99) imply a calc-

Table 3
Chemical composition of MMEs and the host monzogranites.

Monzogranites												
Samples	GRC-1	3	4	8	11	13	16	18	21	22	74	76
wt%												
SiO_2	68.36	68.04	68.07	67.10	67.91	73.90	68.10	70.42	71.18	71.95	68.33	68.21
TiO_2	0.39	0.42	0.42	0.42	0.41	0.16	0.40	0.34	0.40	0.29	0.43	0.39
Al_2O_3	15.17	15.21	15.16	15.69	15.26	14.29	14.97	15.11	14.17	13.96	15.17	15.45
FeO^t	2.73	2.93	2.92	3.00	2.88	0.89	3.69	1.61	2.14	1.73	2.88	2.61
MnO	0.07	0.07	0.07	0.08	0.08	0.03	0.12	0.04	0.04	0.06	0.08	0.07
MgO	0.94	0.99	1.04	1.05	1.00	0.29	1.32	0.69	0.96	0.49	1.04	0.89
CaO	2.71	2.72	2.60	2.71	2.73	0.81	3.18	1.86	2.23	1.55	2.56	2.61
Na_2O	4.58	4.56	4.46	4.42	4.54	4.90	4.31	5.15	4.87	4.20	4.49	4.57
K_2O	3.51	3.31	3.60	4.04	3.62	3.97	1.61	3.65	3.02	4.47	3.51	3.81
P_2O_5	0.13	0.14	0.14	0.14	0.14	0.04	0.14	0.12	0.11	0.07	0.14	0.13
LOI	1.02	1.10	1.10	0.98	1.02	0.45	1.50	0.42	0.70	1.02	1.01	0.90
Total	99.91	99.82	99.90	99.96	99.91	99.83	99.75	99.59	100.06	99.98	99.96	99.93
ppm												
Ni	–	–	–	–	–	–	–	5.70	12.40	–	–	13.90
Cr	–	–	0.40	0.50	–	4.30	1.80	19.10	12.70	–	6.00	12.60
V	46.32	63.30	55.07	60.42	52.30	18.80	57.28	44.62	45.82	31.67	61.76	71.78
Rb	87.80	90.90	98.20	101.90	100.50	113.60	32.00	88.10	112.60	108.20	91.90	101.40
Sr	422.80	429.50	421.60	464.70	435.80	490.60	501.50	892.00	543.80	269.80	474.10	514.30
Ga	24.94	26.04	24.14	24.35	22.43	38.88	17.54	29.91	25.63	25.91	25.28	12.22
Y	16.85	13.32	16.08	13.45	14.56	9.87	17.00	6.49	10.59	18.02	17.62	8.43
Nb	10.57	11.87	10.46	10.57	11.69	9.46	4.58	5.74	9.31	13.29	11.49	9.82
Zr	192.41	158.49	177.09	149.64	178.21	104.74	121.64	143.27	128.90	147.85	188.16	70.74
Ba	840.19	798.49	865.58	1082.38	900.06	857.95	642.36	912.37	521.52	844.65	1018.41	279.36
Cs	3.41	3.03	3.68	3.22	3.17	5.45	1.47	4.34	4.69	3.49	3.92	3.31
Hf	4.51	3.78	4.56	3.52	4.48	3.39	3.12	3.34	3.88	3.96	4.58	1.43
Ta	1.20	0.75	0.99	0.73	0.85	1.21	0.29	0.46	0.74	1.25	0.76	0.20
Pb	20.54	29.09	24.90	24.77	16.86	53.07	9.10	26.77	23.19	35.08	23.17	6.08
Th	11.42	8.77	11.47	11.30	9.93	9.81	2.29	5.45	17.02	12.52	12.02	0.98
U	4.07	3.25	3.44	3.80	3.97	3.28	0.69	1.79	4.01	4.92	3.43	0.86
La	25.00	22.83	23.57	24.41	22.48	18.70	11.83	19.95	21.97	24.85	28.95	8.52
Ce	50.10	49.30	46.70	48.41	48.15	36.64	24.46	39.55	42.98	56.44	58.05	20.74
Pr	5.67	5.21	5.07	5.17	5.08	4.19	2.80	4.43	3.11	6.14	6.17	2.39
Nd	21.91	19.14	21.05	20.25	20.37	16.64	12.36	15.91	17.14	23.31	24.61	10.72
Sm	4.29	3.47	4.13	3.77	3.41	2.94	2.66	3.08	3.10	4.26	4.67	2.21
Eu	1.34	0.92	1.00	0.94	1.08	0.67	0.91	0.69	0.81	0.90	1.07	0.41
Gd	3.08	2.32	2.71	2.36	2.93	2.12	2.12	1.89	2.61	3.33	3.35	1.63
Tb	0.76	0.37	0.42	0.40	0.40	0.29	0.49	0.23	0.30	0.50	0.46	0.25
Dy	3.01	2.34	2.87	2.19	2.56	1.83	2.91	1.48	1.40	3.06	3.20	1.52
Ho	0.81	0.47	0.54	0.43	0.49	0.30	0.49	0.19	0.29	0.62	0.59	0.31
Er	2.12	1.33	1.38	1.40	1.27	0.90	1.74	0.63	0.86	1.54	1.51	0.84
Tm	–	0.22	0.25	0.20	0.22	0.12	0.35	0.09	0.14	0.33	0.27	0.11
Yb	–	1.49	1.66	1.10	1.58	0.69	1.78	0.65	0.86	2.10	1.41	0.78
Lu	0.62	0.20	0.23	0.26	0.27	0.15	0.29	0.10	0.16	0.25	0.24	0.14

MMEs												
#	GRC-1EN	3 EN	4 EN	8 EN	9 EN-A	10EN	11EN	12EN	13EN	16EN	18EN	18EN-R
wt%												
SiO_2	51.47	60.03	63.65	55.88	58.23	57.41	55.87	56.92	50.67	61.61	58.47	55.95
TiO_2	0.97	0.77	0.80	0.86	0.67	1.04	0.93	0.88	1.25	0.58	0.79	0.63
Al_2O_3	24.96	16.60	15.54	17.28	17.48	16.74	17.06	16.06	18.08	16.91	16.02	17.53
FeO^t	5.79	5.70	4.50	7.07	5.90	6.84	7.68	6.68	9.33	5.68	6.24	6.47
MnO	0.18	0.17	0.08	0.22	0.15	0.20	0.21	0.23	0.28	0.21	0.19	0.19
MgO	1.34	2.29	2.63	3.14	2.17	3.08	3.40	3.62	4.04	1.89	2.77	1.48
CaO	3.18	3.56	2.53	5.12	4.72	4.44	3.95	5.44	6.22	3.85	5.38	8.56
Na_2O	5.82	5.87	5.52	5.24	5.58	5.23	5.38	4.69	5.14	6.14	5.44	4.82
K_2O	3.21	2.38	2.16	2.22	2.19	2.55	1.78	2.26	1.88	1.15	2.14	0.76
P_2O_5	0.27	0.22	0.28	0.24	0.32	0.33	0.25	0.29	0.41	0.23	0.30	0.21
LOI	2.01	1.72	1.45	2.11	1.76	2.10	2.43	2.32	1.56	1.42	1.50	2.52
Total	99.85	99.94	99.64	100.17	99.83	100.72	99.80	100.13	99.90	100.30	99.93	99.84
ppm												
Ni	32.60	–	52.80	3.70	–	20.90	2.60	39.80	–	–	6.60	–
Cr	43.70	–	106.90	21.50	1.70	30.90	0.40	99.60	–	–	4.50	2.30
V	159.63	101.75	85.00	141.87	100.40	122.71	147.50	126.81	117.14	70.08	126.10	92.26
Rb	187.60	124.20	112.20	118.60	99.90	135.40	151.20	96.80	89.10	25.50	69.40	17.30
Sr	290.20	395.80	834.80	452.70	490.60	333.80	444.90	528.20	434.40	448.40	590.00	761.60
Ga	35.13	23.96	31.08	24.85	25.89	27.63	29.32	23.11	56.07	19.18	20.67	27.97
Y	42.83	22.91	10.86	21.74	19.57	15.73	16.63	19.94	34.67	51.19	21.40	49.20
Nb	24.22	20.39	10.71	18.26	13.78	19.32	23.78	14.55	24.89	7.30	13.83	9.62
Zr	415.29	211.22	191.05	139.08	180.88	178.29	145.20	157.63	403.28	46.37	163.55	43.25
Ba	888.86	553.90	338.85	497.84	454.87	525.24	470.53	506.16	2426.25	439.49	572.76	205.61

Table 3 (*continued*)

#	MMEs GRC-1EN	3 EN	4 EN	8 EN	9 EN-A	10EN	11EN	12EN	13EN	16EN	18EN	18EN-R
Cs	13.00	3.88	8.04	5.29	4.63	9.43	8.56	4.11	8.63	1.12	3.65	0.66
Hf	11.38	6.56	4.64	4.24	4.91	4.92	4.26	4.39	9.53	1.60	4.46	1.49
Ta	2.10	1.33	0.76	0.88	0.84	1.12	1.30	0.75	1.58	0.45	1.00	0.36
Pb	60.60	17.08	14.05	14.58	16.61	16.45	10.20	13.18	55.19	8.77	13.56	11.03
Th	30.10	9.88	6.03	9.70	13.83	13.45	8.65	12.19	19.45	5.01	13.12	2.76
U	3.39	7.78	1.93	7.84	9.49	11.19	11.71	4.17	5.96	1.33	13.12	1.26
La	76.00	24.46	34.21	21.62	27.62	26.98	18.75	23.72	49.63	25.85	35.51	14.99
Ce	130.54	46.68	61.62	40.32	51.20	50.52	40.30	49.58	97.72	54.09	70.71	31.61
Pr	15.91	5.24	6.71	5.05	5.23	5.45	4.32	6.16	10.75	7.01	8.23	4.92
Nd	61.87	21.75	26.86	21.06	20.21	19.57	17.77	27.21	44.70	33.05	32.15	25.13
Sm	10.47	4.24	3.97	4.39	4.00	4.08	3.44	5.26	8.29	8.05	6.06	8.16
Eu	2.07	0.88	1.17	0.88	0.82	1.01	0.76	1.20	2.35	1.34	1.71	1.01
Gd	7.46	3.47	2.25	3.78	3.30	2.97	2.72	3.94	5.75	8.02	4.38	6.43
Tb	1.10	0.54	0.36	0.53	0.47	0.50	0.40	0.59	1.05	1.34	0.59	1.29
Dy	6.80	3.59	1.90	3.27	3.08	2.74	2.58	3.44	5.91	9.18	3.82	8.27
Ho	1.36	0.73	0.32	0.63	0.68	0.64	0.49	0.63	1.20	1.75	0.70	1.75
Er	3.57	2.13	1.01	2.24	1.78	1.64	1.57	1.92	3.27	5.17	1.97	4.97
Tm	0.55	0.42	0.15	0.34	0.31	0.28	0.26	0.31	0.58	0.77	0.34	0.65
Yb	3.37	2.70	0.86	2.29	2.11	1.79	1.93	2.02	3.69	5.14	1.99	4.60
Lu	0.65	0.55	0.17	0.46	0.47	0.37	0.31	0.34	0.62	0.71	0.41	0.71

#	MMEs GRC-19EN	21EN	22EN	22EN-A	74EN	76EN
	wt%					
SiO_2	62.67	61.24	63.02	66.28	57.87	65.12
TiO_2	0.84	0.52	0.75	0.73	0.90	0.52
Al_2O_3	15.52	17.03	16.79	15.50	17.16	16.39
FeO^t	4.98	4.71	4.22	3.10	5.89	4.18
MnO	0.10	0.12	0.09	0.10	0.17	0.12
MgO	3.33	1.78	1.66	1.03	2.52	1.21
CaO	2.46	4.22	4.24	2.43	5.14	4.38
Na_2O	5.44	5.57	5.28	5.12	5.26	4.40
K_2O	2.52	2.49	2.16	4.30	2.20	1.51
P_2O_5	0.27	0.33	0.20	0.21	0.36	0.15
LOI	1.22	1.23	1.01	0.90	1.60	1.12
Total	99.91	99.77	99.89	100.04	99.73	99.56
	ppm					
Ni	179.40	–	10.10	–	8.00	134.80
Cr	102.19	68.35	56.80	44.66	113.28	171.89
V	132.90	93.90	71.50	101.60	92.80	125.50
Rb	707.20	525.10	623.00	464.10	688.40	509.60
Sr	33.98	25.15	40.20	13.08	25.63	68.29
Ga	6.08	18.48	53.11	17.35	19.39	21.95
Y	8.06	11.53	25.91	8.16	15.73	21.00
Nb	157.58	181.18	577.68	174.65	155.78	281.52
Zr	288.16	501.15	2067.36	414.84	580.44	489.31
Ba	10.45	3.05	4.56	1.77	5.68	27.41
Cs	4.00	4.92	13.43	3.87	4.18	7.92
Hf	0.49	1.05	2.04	0.71	0.98	1.11
Ta	14.16	18.04	92.66	12.27	12.86	37.77
Pb	8.56	15.12	24.55	4.76	13.44	14.12
Th	2.68	5.53	8.99	1.97	9.00	4.33
U	41.65	25.50	59.22	18.08	30.45	33.01
La	58.31	54.84	123.29	39.12	57.62	78.55
Ce	4.78	6.31	14.21	4.73	5.89	8.74
Pr	16.91	23.93	63.33	20.91	23.92	39.03
Nd	2.48	4.34	13.60	4.21	4.65	7.69
Sm	0.90	1.01	3.79	0.82	1.23	1.28
Eu	1.66	3.71	10.83	3.21	3.58	5.28
Gd	0.20	0.49	1.62	0.54	0.60	0.76
Tb	1.00	3.13	9.22	3.15	3.23	4.10
Dy	0.22	0.73	1.75	0.58	0.70	0.69
Ho	0.58	1.78	4.65	1.72	1.72	1.88
Er	0.11	0.34	0.80	0.27	0.30	0.36
Tm	0.64	2.23	4.87	1.57	2.08	1.96
Yb	0.09	0.43	0.88	0.26	0.38	0.14
Lu	62.67	61.24	63.02	66.28	57.87	65.12

alkaline to alkali-calcic character for these rocks (Frost et al 2001). Both rock types are strongly metaluminous (I-type granites), except three samples with a mildly peraluminous character. Their Alumina Saturation Index (ASI) ranges from 0.72 to 1.03 (Supplementary Item-I, Fig. S7c). All the MMEs and monzogranites exhibit an I-type character on a Na_2O *vs* K_2O plot of Chappell and White (1992) (Supplementary Item-I, Fig. S7d).

The primitive mantle-normalized patterns of the MMEs and
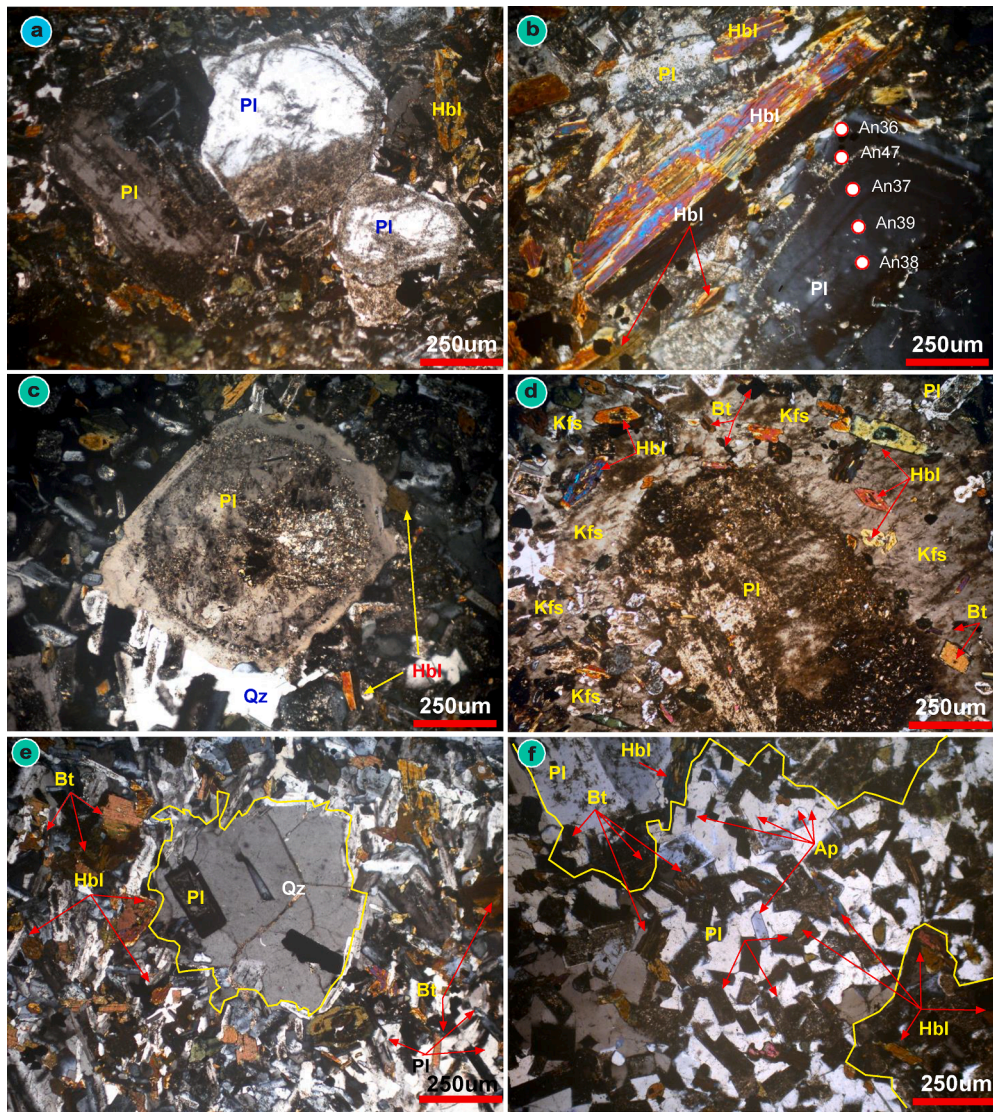
Fig. 3. Photomicrographs show textural features of the MMEs; (**a**) Cluster of rounded to elongated plagioclase phenocrysts forming glomeroporphyritic texture. These phenocrysts are highly sericitized and altered on the outer rims, (**b**) complex-growth zoned plagioclase phenocryst overprinted by alteration, whereas individual growth zones (showing An content corresponding to analysis spots) of varying thickness and curved corners are truncated against a dissolution surface. It encloses acicular hornblende on the outer rim and is associated with large flaky hornblende with some alteration into chlorite. The An content represents the abrupt change in plagioclase composition toward outer rim, (**c**) Plagioclase phenocrysts show spongy core and clear mantle and corroded and desorbed outer zone, (**d**) Sericitized plagioclase phenocryst has an outer rim of K-feldspar enclosing fine-grained biotite flakes and prisms of plagioclase and hornblende, (**e**) Large irregular ocelli phenocryst of quartz rimmed by fine-grained plagioclase, hornblende, and biotite, (**f**) Anhedral phenocryst of quartz containing fine inclusions of plagioclase laths, which are associated with biotite and hornblende, (**g**) Elongated acicular hornblende indicating quenching of mafic magma blob, (**h**) Tabular and six-sided phenocrysts of hornblende with patchy domains and altered cores into epidote, (**i**) Aggregates of hornblende and biotite together with Fe-Ti oxides and accessory minerals forming mafic clots circled by feldspar and quartz, (**j**) Acicular apatite included in quartz, (**k**) Acicular elongated needle-shaped apatite occurs as inclusions in quartz and indicates clear quenching of the mafic melt globules trapped in silicic magma, and (**l**) Wedge-shaped large crystals of titanite associated with quartz, plagioclase and chlorite. Abbreviation: Hornblende (Hbl); Biotite (Bt); Plagioclase (Pl); and K-feldspar (Kfs); Epidote (Ep); Acicular apatite (Ap); Quartz (Qz); Titanite (Ttn); Zircon (Zrn); Opaques (Opq).

monzogranites (Fig. 7a-b) show pronounced Nb, Ti, and P troughs and Pb and K peaks. In general, they are strongly enriched in light rare earth elements (LREE) and large-ion lithophile elements (LILE), such as Rb, Sr, Ba, U, and K. They are relatively depleted in heavy rare earth elements (HREE) and the high field strength elements (HFSE) Y, Nb, Ta, and Zr (and Hf). However, the MMEs despite their more mafic composition exhibit higher contents of U, Th, Nb, Zr and REEs compared to the host monzogranites and other less mafic MMEs (see Fig. 13b). The higher REE concentrations in the mafic MMEs compared to the more evolved intermediate MMEs is discussed later (Section 9).

The prominent negative anomalies of Nb, P, and Ti, and the strong

positive Pb anomaly are typical signatures of subduction-related magmas in continental arc- or crustal-derived melts (Wilson, 1989). Chondrite-normalized REE patterns for the MMEs and the monzogranites have similar topologies, however, the LREE/HREE ratios ($(La/Yb)_N = 1.97–39.65$ for the MMEs and 4.02–18.74 for monzogranites) indicate they are variably fractionated. Both the MMEs and host rock show negative Eu anomalies (Eu/Eu* for monzogranites: 0.62–0.94, > 1.00 in three samples; for MMEs: 0.41–0.98, > 1.00 in two samples) (Fig. 7c, d). Both rock types exhibit moderately fractionated LREE patterns ($La_N/Sm_N = 1.13–5.3$ in the MMEs and 2.4–5.6 in the monzogranites) and nearly flat HREE patterns ($Gd_N/Lu_N = 0.77–2.3$ in
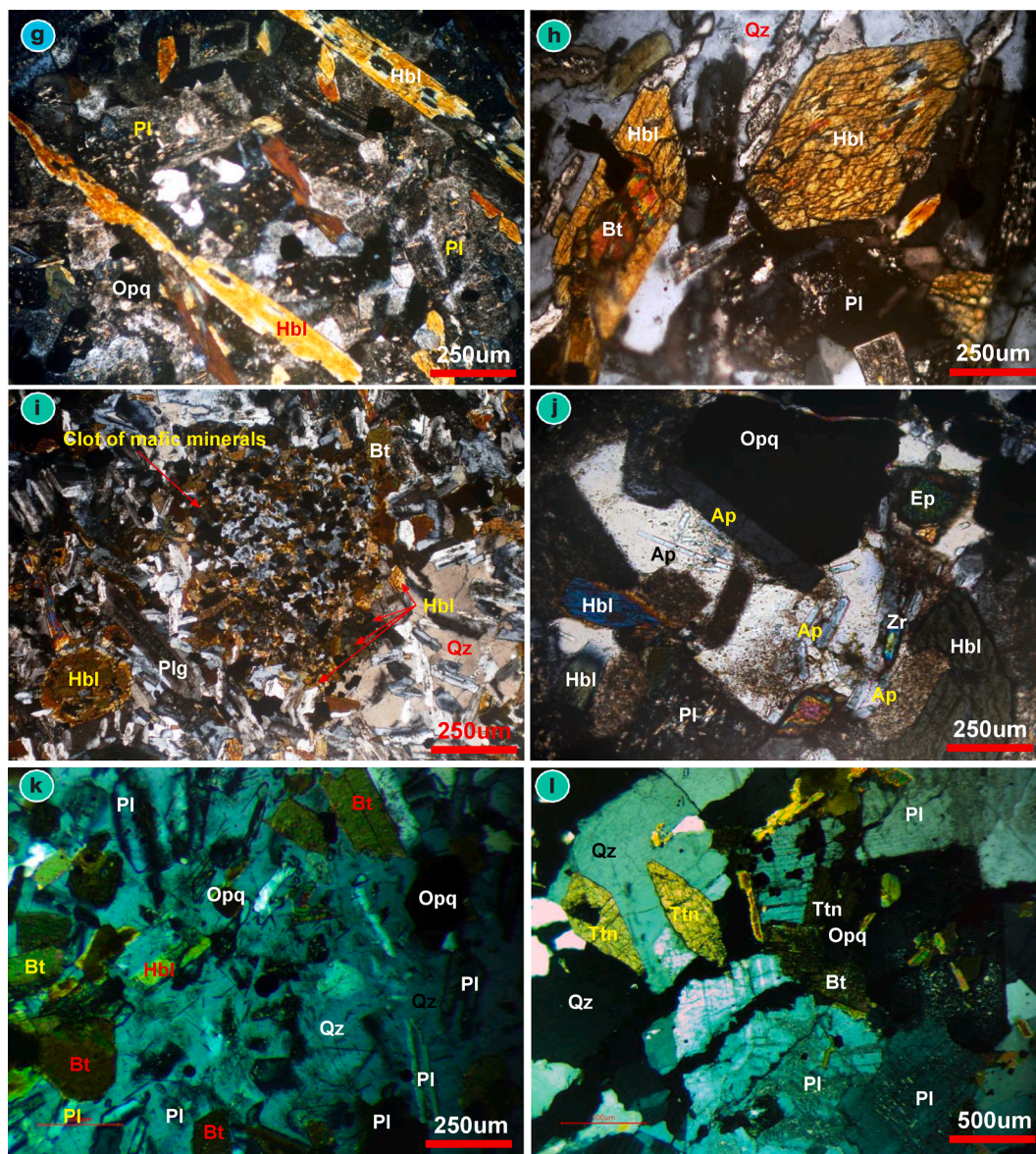
Fig. 3. (continued).

the MMEs and 0.6–2.3 in the monzogranites).

6.1. Apatite REE composition

The REE and some trace elements of apatite from the MME sample GRC-21EN and the monzogranite sample GRC-21 (Supplementary Item-III, Table S6) reveal compositional homogeneity, except for three apatites from the MME that likely represent xenocrysts. Excluding three xenocrysts, the apatite from the MMEs and host monzogranite exhibit similar chondrite- normalized REE patterns (Fig. 7e, f), similar δEu values (*av.* 0.47 and 0.39) and δCe values (*av.* 1.05 and 1.08), ΣREE contents (4861 and 4588 ppm), and degree of LREE/HREE fractionation (La_N/Lu_N = 18.43 and 28.34), respectively. Other trace elements (e.g., Sr, Y, Zr) also exhibit very similar values. In contrast, the inferred xenocrysts are highly depleted in REE with fractionated LREE patterns and nearly flat HREE patterns.

7. Whole-rock Sr-Nd isotopic composition

Whole-rock Sr-Nd isotopic analyses of representative samples of the MMEs and the host monzogranites are given in Table 4 and the

analytical method is described in Supplementary Item-II, Section 3. Initial $^{87}Sr/^{86}Sr$ ratios (SrI) of the MMEs are generally low ranging from 0.70302 to 0.70373, while those of the monzogranites range from 0.70302 to 0.70407. The initial $^{87}Sr/^{86}Sr$ values for both the MMEs and the monzogranites overlap or are very similar. The initial $^{143}Nd/^{144}Nd$ (NdI) ratios of the MMEs range from 0.512518 to 0.512586 and are very similar to the monzogranites values (0.51198–0.51201). Both the MMEs and monzogranites show positive εNd(t) values of + 3.49 to + 5.45 and + 2.29 to + 4.57, respectively. Figure (8) shows the evolution of εNd(t) *vs.* age data for the MMEs and their host monzogranites compared to the western and eastern terranes of the Arabian Shield (Stoeser and Frost, 2006) and the northernmost ANS (Stein and Goldstein, 1996; Stern, 2002; Moussa et al., 2008). The εNd(t) values for the MMEs and monzogranites plot below the depleted mantle evolution curve of DePaolo (1981) and Goldstein et al. (1984).

8. Discussion

8.1. Magmatic processes

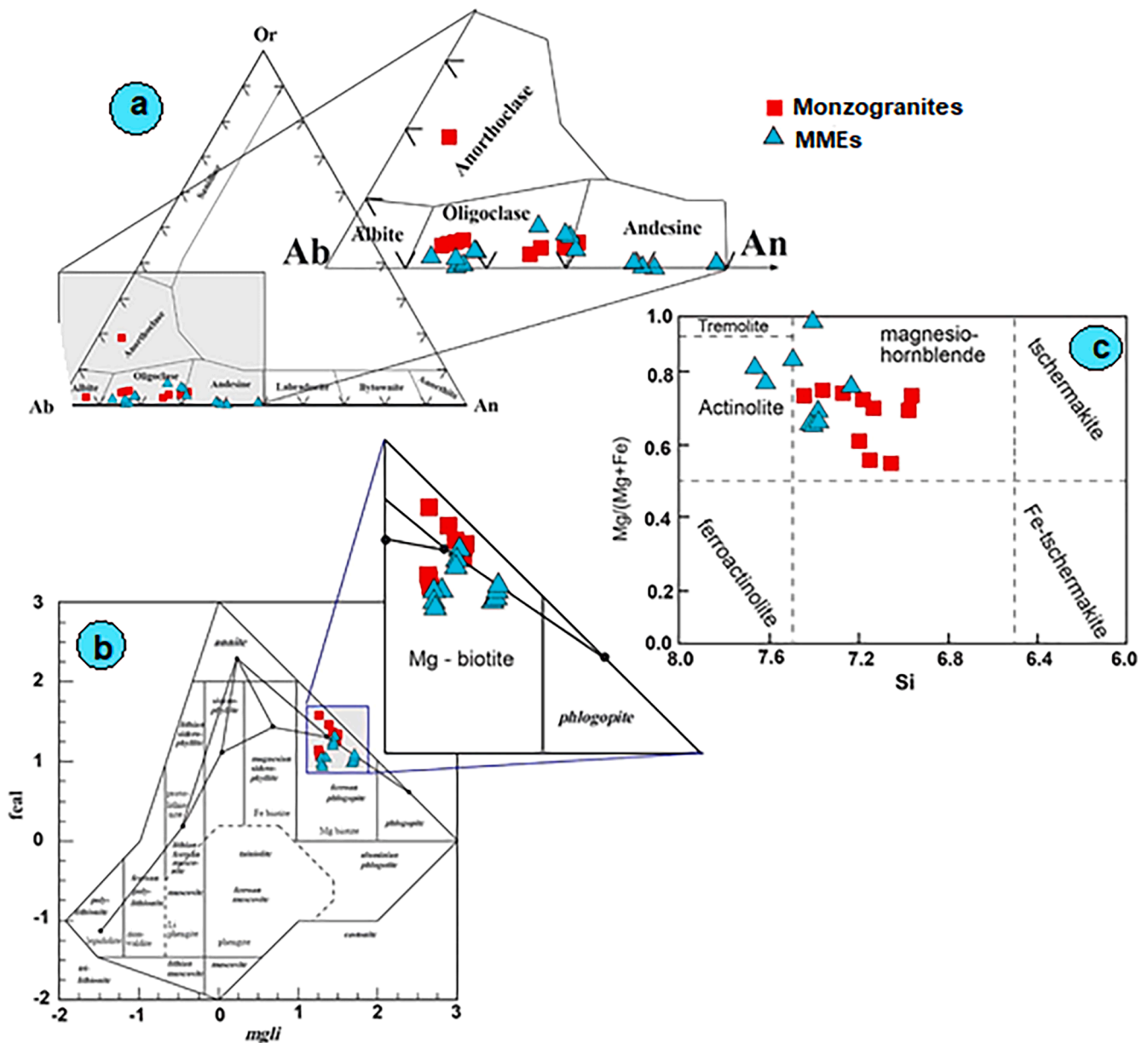Solid inclusions or components within the granites may consist of

Fig. 4. Chemical classification of (a) plagioclases of the monzogranites and MMEs using Ab-Or-An triplot, **(b)** biotites on $(Fe^t + Mn + Ti + Al^{VI})$-(Mg-Li) diagram (Tischendorf, et al., 1997), (c) amphibole on scheme of Leake et al. (1997). The same symbols of monzogranites and MMEs are used in the next figures.

primary crystals, which crystallized directly from the melt phase, unmelted or partially melted crystals (restite) derived from the source rock, and other larger polymineralic inclusions, collectively known as enclaves (Didier, 1973; Vernon, 1983). Among the main genetic models proposed for mafic microgranular enclaves, include (i) the xenolith model (e.g., Bateman 1995; Kumar et al., 2004; Zafar et al., 2020); (ii) the restite model (e.g., Chappell et al. 1987; Chen et al., 1989); (iii) the autolith or cognate model (e.g., Blundy and Sparks 1992; Kumar, 2010; Perugini et al., 2003 Perugini et al., 2004); and (iv) the magma mixing/mingling model (Vernon, 1984; Poli and Tommasini 1991; Kumar et al., 2004; Sarjoughian et al., 2019; Poli et al., 2020; Dou et al., 2021; Barnes et al., 2021). More weight is given to magma mixing/mingling processes, which are common in calc-alkaline plutonic systems associated with subduction zones and post-collisional settings (e.g., Kumar, 2010; Pascual et al., 2008; Bora et al., 2013), and create features like zoned MMEs (Adam et al., 2019).

The first scenario, i.e., xenolith model, is considered not applicable for the present MMEs due to the absence of contact aureoles,

metamorphic fabrics, and cross-cutting relationships with the host rock, and the frequent presence of feldspar phenocrysts/megacrysts in the peripheral parts of the monzogranites and within the MMEs. In the restite model, the MMEs are thought to represent residual or unmelted metasedimentary or igneous sources after partial melting to produce granite magma (e.g., Chappell and White, 1992; Collins, 1998; White et al., 1999). However, the MMEs clearly lack reaction signatures or metamorphic textures and are devoid of residual or new mineral phases (e.g., garnet, sillimanite, cordierite, etc.). Neither do the monzogranites carry any peritectic entrained assemblages; rather primary phases are present as crystallization products. Their elliptical shape implies plastic (semi-solid) deformation of rounded to subrounded MMEs due to stretching within the partially crystallized felsic magma system under the influence of magmatic flow without any or minimal solid-state deformation, which indicates the coeval nature of crystal-charged felsic and mafic magmas before their solidification (e.g., Kumar et al., 2004). Furthermore, the typical igneous textures including fine-grained to porphyritic, poikilitic, interstitial texture plus mineral magmatic
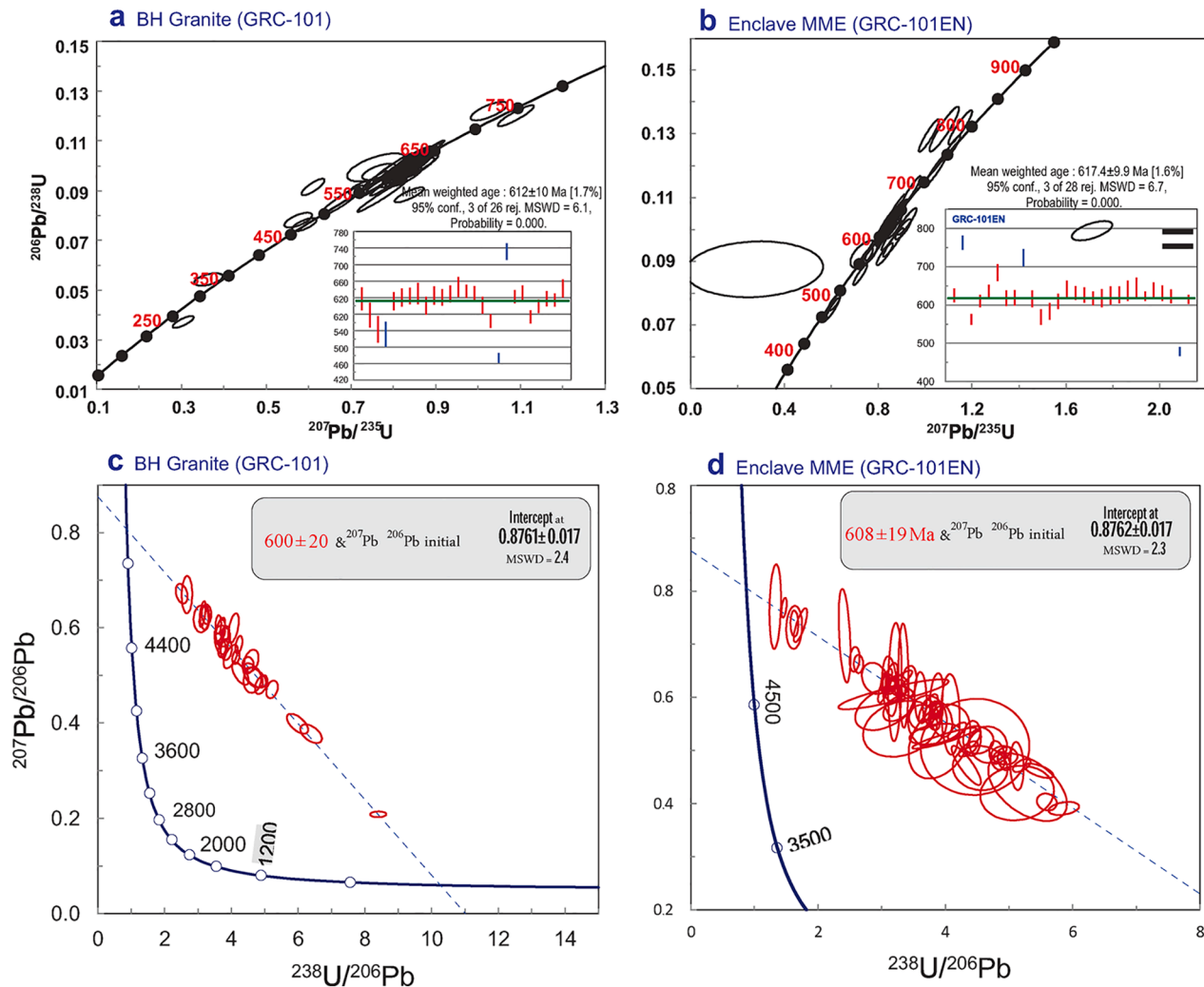
Fig. 5. U–Pb ages Concordia of zircon for (**a**) the host monzogranites and (**b**) MMEs, and U–Pb ages Concordia of apatite for (**d**) the host monzogranites and (**e**) MMEs from the Gharib granitoids complex.

zonation and sharp contacts with the monzogranite, rule out a restite origin for the MMEs from GGC.

The low content of mafic minerals (<50 vol%) and non-cumulative nature of the MMEs from the GGC do not support the autolith (cognate or cumulate) model as argued elsewhere (e.g., Weinberg et al., 2001; Xiao et al., 2020). According to this model (e.g., Dodge and Kistler, 1990), the mafic chilled margins can be broken into fragments comparable to MMEs (Fernández and Castro, 2018; Donaire et al., 2005), when host magma move through the same conduit. This mechanism will produce equigranular coarse-grained cumulate-like textures, which are absent in our samples. Instead, they exhibit fine-grained textures with abundant needle- and stubby forms of apatite implying rapid cooling of host magma by intrusion into magmas of lower temperature.

One of the new models recently suggested for MMEs formation in plutonic rocks (Rodríguez and Castro 2017, 2019) is based on the geochemical and isotopic similarity between MMEs and host monzogranites, similar to that of cognate model, and ascribed to magma differentiation during ascent along conduits. Crystallization would occur on the walls of the magma conduits through which the granitic magmas were emplaced in the upper crust. This process can be considered as an alternative hypothesis to magma mixing for the generation of some microgranular enclaves, especially where no direct evidence exists for the presence of mafic magmas coeval with granitoids, and there is a lack of geochemical and isotopic contrast between monzogranites and MMEs.

Several lines of evidence discussed in the following sections, support the mafic-felsic magma interaction (i.e., mixing, mingling, and supercooling), as the most viable origin for the MMEs in monzogranites from the GGC. Different approaches have been taken to decipher the role of magma mixing/mingling process in the origin of plutonic MMEs in the literature, which focus on either a detailed study of mineral compositions and zoning (e.g., Barnes et al., 2021; Adam et al., 2019; Dou et al., 2021), whole-rock geochemical and isotopic data (e.g., Poli et al., 2020), field (e.g., Kumar et al. 2004), and microstructural evidence (e.g., Vernon, 1990; Vernon, 1991; Kumar, 2010), or combination of these approaches (e.g., Rodríguez and Castro, 2019). This study integrates field observations, petrography, mineral chemistry, and whole-rock geochemical and isotopic data to model the origin of the MMEs in monzogranites from the GGC.

8.1.1. Field criteria supporting the magma mixing/mingling model

The occurrence of mafic and felsic magmatism in the form of basaltic and rhyolitic dykes together with intermediate andesitic magmas in the study area and nearby in this part of the NED (Stern et al., 1984), raise the possible role of magma mixing and mingling processes in the genesis of ubiquitous MMEs in the monzogranites. The sharp, crenulated (pillow-like) contacts of MMEs with felsic host (Fig. 2c, e, f, g, i), indicate interaction between melts of contrasting compositions. In a few MMEs, fine-grained quenched margins (Fig. 2g) are noticeable, indicating rapid
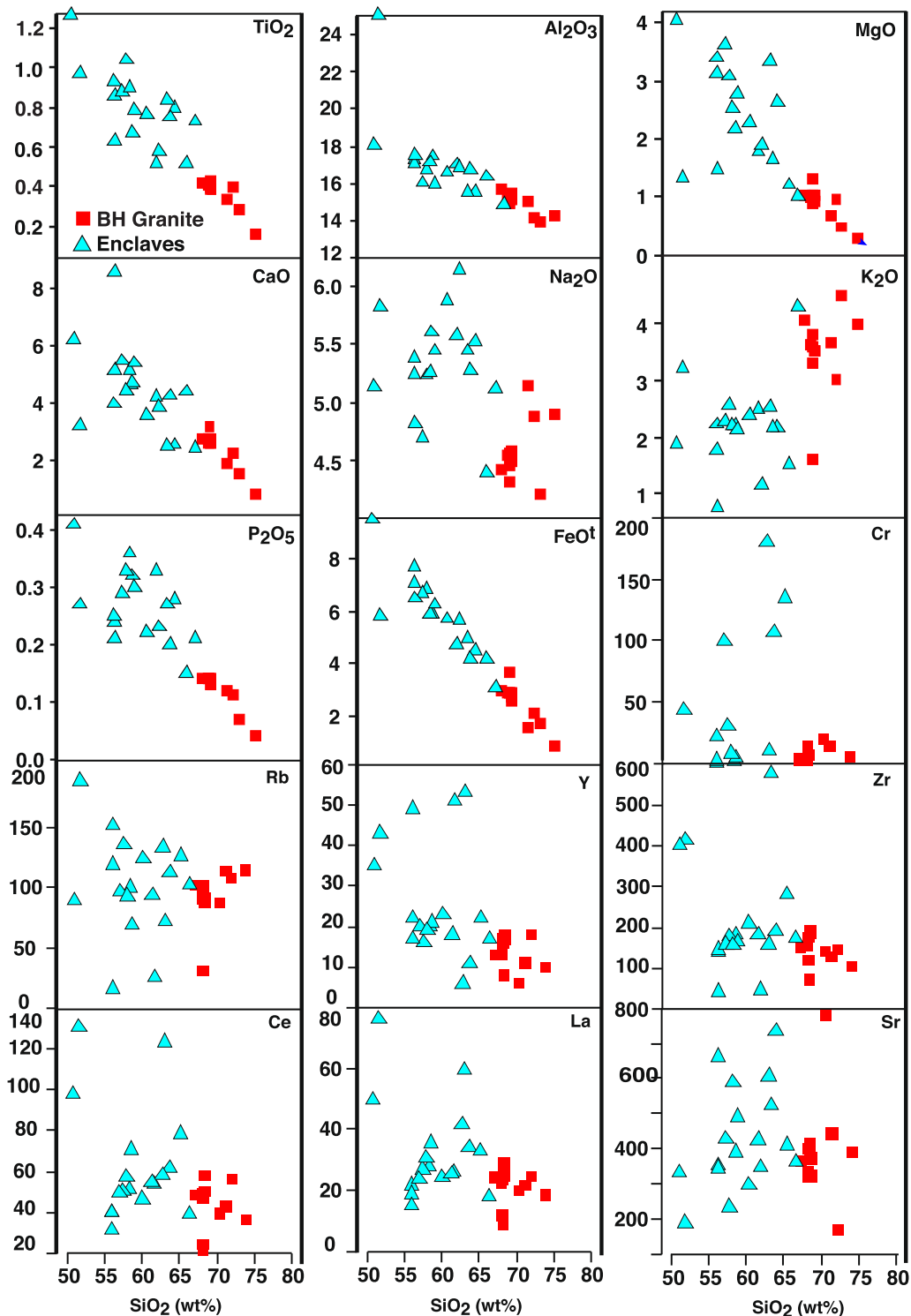
Fig. 6. Variations plots of some selected major, minor, and trace elements against SiO_2 for the monzogranites and MMEs in the Gharib complex.

cooling or quenching of the MME magma and implying their injection as melts and/or crystal-charged melts into the partially liquid host magmas.

Indeed, diverse elongated, rounded, and ellipsoidal to stretched morphologies of the MMEs within monzogranites most likely resulted from mechanical dilution (disintegration) of large-sized mafic globules into several smaller ones during the interaction with the host felsic magma prior to the complete homogenization, i.e., mixing.

Interacting magmas with different rheologies can easily create chaotic patterns (e.g., Perugini and Poli, 2000), which are indicated by the presence of fractal structures in our MMEs. The magmatic deformation of these MMEs is often reflected by: (i) magmatic flow fabrics of the host felsic melt inferred by lenticular enclaves (Fig. 2a, d, e, k) and (ii) chaotic dynamic or viscous finger flow of the enclave magma recognized by irregular-shaped enclaves with wispy tails and disaggregated smaller ones (Fig. 2d, i-l) (Perugini and Poli, 2000; Kumar, 2010; Renjith et al., 2013).

Parallel alignment of flattened, elongated, and stretched MMEs
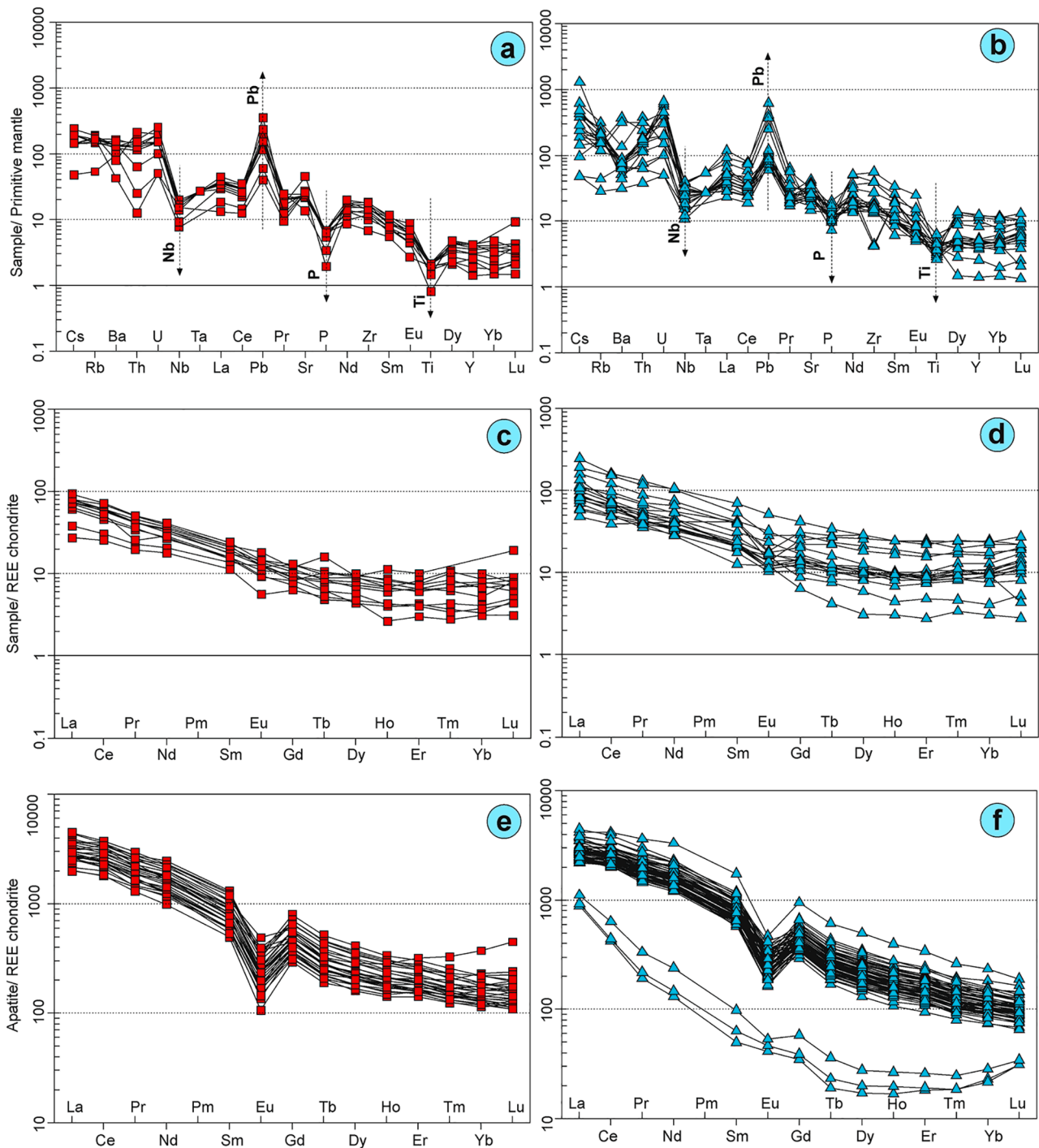
Fig. 7. Spider diagrams normalized to the primitive mantle of Sun and McDonough (1989) for (**a**) the monzogranites and (**b**) the MMEs. Rare earth elements patterns normalized to Chondrite (Sun and McDonough, 1989) for (**c**) the monzogranites and (**d**) the MMEs. Rare earth elements patterns of apatites normalized to Chondrite (Sun and McDonough, 1989) for (**e**) the monzogranites and (**f**) the MMEs.

within the host monzogranites implies magmatic fabric flow (Fig. 2j). It is inferred that the chaotic dynamic rotation movement and stretching of mafic blobs within the host felsic magma have developed a schlieren tail and fragmentation of larger MMEs into smaller rounded/sub-rounded ones (Fig. 3i, k; 9a). Such stretching and folding mechanisms enhance mechanical transfer (mingling) and mixing, in which the two melts can exchange components via non-linear coupled processes (e.g., Pesquera and Pons, 1989; De Campos et al., 2008; De Campos et al., 2011).

Since the chemical composition of mafic magma (MME) is not suitable to crystallize K-feldspar phenocrysts, the common occurrence of

large-grained K-feldspar in MMEs and host monzogranites (Fig. 2e, i) indicates the possibility of mechanical transfer of minerals (e.g., Paterson et al., 2006). The presence of feldspar phenocrysts cross-cutting the MMEs–host boundaries (Fig. 2i), supports mechanical transfer of feldspar into the enclave magma from the partially crystallized host magma, most likely during mingling of MME globules (e.g., Vernon et al., 1988; Kumar et al., 2005). The mechanism under which the phenocrysts are captured from the partially crystallized felsic magma and entrain into the mafic enclave magma is explained in Fig. 9a, where forces associated with magmatic deformation, such as the shear stress of the host magma

Table 4
Sr-Nd isotopes of the MMEs and the host BH granites.

	GRC-8	GRC-10EN	GRC-11	GRC-12EN	GRC-13	GRC-13EN	GRC-18	GRC-18EN	GRC-21	GRC-21EN
$^{87}Sr/^{86}Sr$	0.70855	0.71344	0.70978	0.70812	0.70895	0.70881	0.70565	0.70597	0.70820	0.70745
Rb Cont	101.9	135.4	100.5	96.8	113.6	89.1	88.1	69.4	112.6	93.9
Sr Cont	464.7	333.8	435.8	528.2	490.6	434.4	892.0	590.0	543.8	525.1
t (Ma)	600	600	600	600	600	600	600	600	600	600
$^{87}Rb/^{86}Sr$	0.63549	1.17555	0.66832	0.53111	0.67106	0.59442	0.28623	0.34089	0.60008	0.51824
SrI	0.70312	0.70338	0.70407	0.70357	0.70320	0.70373	0.70320	0.70305	0.70306	0.70302
eSr	−9.63	−5.84	3.88	−3.1	−8.4	−0.9	−8.4	−10.53	−10.4	−11.05
$^{143}Nd/^{144}Nd$	0.51250	0.51254	0.51250	0.51255	0.51248	0.51259	0.51244	0.51252	0.51246	0.51252
Sm Cont	3.77	4.08	3.41	5.26	2.94	8.29	3.08	6.06	3.10	4.34
Nd Cont	20.25	19.57	20.37	27.21	16.64	44.70	15.91	32.15	17.14	23.93
t (Ma)	600	600	600	600	600	600	600	600	600	600
$^{147}Sm/^{144}Nd$	0.1126	0.1259	0.101	0.1168	0.1066	0.1121	0.1169	0.1139	0.1094	0.1095
NdI	0.51206	0.51204	0.51210	0.51209	0.51206	0.51215	0.51198	0.51207	0.51203	0.51209
eNd	3.72	3.45	4.57	4.39	3.86	5.49	2.29	4.01	3.18	4.35

or the stress developed due to the compaction of overlying crystal-rich mush in the absence of flow fabrics in the surrounding host matrix, play a major role (Fig. 8).

8.1.2. Petrographic features supporting magma mixing/mingling

Several microscopic textural criteria support the mechanical transfer of minerals from the felsic host magma to MMEs, which strongly support a magma mixing/mingling origin. The parallel alignment of long prismatic/tabular/skeletal hornblende, biotite, and plagioclase grains (Fig. 3g) indicates the MMEs were entrained as magma globules of contrasting composition into the host felsic magma. The most important mixing-quench textures and features observed in the MMEs and host monzogranites from the GGC include: (1) Quartz ocelli in the MMEs (Fig. 3e) developed by marginal dissolution and corrosion of quartz phenocrysts, after their entrainment into the MMEs from partially crystallized felsic host magma, under high-T conditions of the host melt (Fig. 9b) (e.g., Baxter and Feely, 2002; Hibbard, 1991; Kumar and Kumar, 2014; Vernon, 1990). The quartz phenocrysts transferred from the felsic magma impose quenching and supercooling conditions to the hot MME magma and induce rapid nucleation and crystallization of fine-grained blade-shaped crystals of plagioclase, biotite, and hornblende (Fig. 9b). (2) The outermost rims of poikilitic K-feldspar phenocrysts in

Fig. 8. The evolution of εNd(t) vs. age data for the monzogranites and associated MMEs in the GGC, along with fields for the Eastern and Western terrane of the Arabian Shield (Stoeser and Frost, 2006), for the northernmost ANS (Stein and Goldstein, 1996; Stern, 2002; Moussa et al., 2008), and for Sinai (Eyal et al., 2010). Reference lines for the chondritic uniform reservoir (CHUR) and the depleted mantle (DM) evolution curves of DePaolo (1981) and Goldstein et al. (1984).
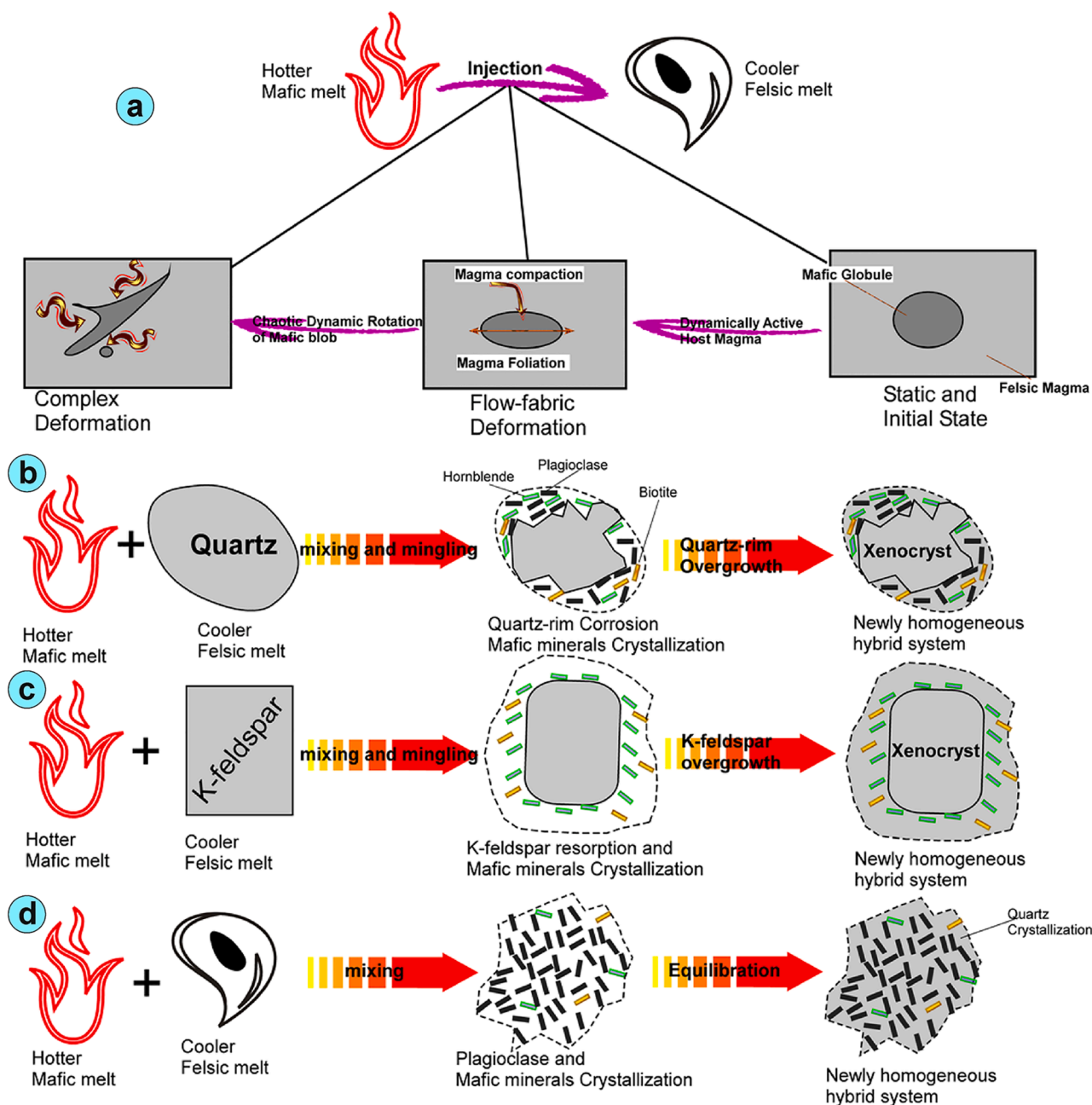
the MMEs (Fig. 3d), might have been formed in a manner similar to that of the quartz ocelli (Vernon, 1991; Hibbard, 1991; Baxter and Feely, 2002). The blade-like biotite and hornblende, overgrowing the partially resorbed surface of K-feldspar phenocrysts, might have grown in a quenched environment (Fig. 9c). (3) Cellular-textured plagioclase phenocrysts in the MMEs (Fig. 3a-d), also imply a mechanical transfer from the felsic host magma to the enclave mafic magma (Silva et al., 2000), during magma mingling or in a mafic-felsic (hybrid) magma zone at depth (Kumar and Rino, 2006). Morphologies like turbid or spongy resorbed, oscillatory zoned plagioclase phenocrysts imply supercooling/quenching processes, whereas clear plagioclase outer margins suggest a slow cooling process (Fig. 3c) (e.g., Lofgren, 1974; Hibbard, 1981). (4) The presence of stubby apatite in the MMEs confirms the mechanical transfer from their felsic host to the mafic enclave magma during mingling processes. Furthermore, the acicular apatite and elongated hornblende and biotite crystals provide strong evidence for supercooling/quenching of hot MME globules within the relatively cooler felsic magma (e.g., Vernon, 1984; 1990; Hibbard, 1995; Kumar, 1995; Baxter and Feely, 2002). (5) Sieve-textures, resorption, and/or the skeletal habit of sub-rounded to rounded plagioclase (Fig. 3c), and hornblende phenocrysts (Fig. 3d, g) indicate disequilibrium growth, during magma mixing process (Choe and Jwa, 2004; Bennett et al., 2019), or rapid decompression in conjunction with magma mixing process (e.g., Nelson and Montana, 1992). The hornblende-biotite clots replaced early crystallized clinopyroxene (Fig. 3i), either indicate disequilibrium growth or represent a concentration of dense early-formed phases (Reid and Hamilton, 1987; Castro, 1990) again supporting magma mixing process. (6) There are two generations of quartz; (a) the interstitial poikilitic crystals which engulfed mafic clots (Fig. 3i), needle-like (acicular apatite, Fig. 3j) and blade-like plagioclase (Fig. 3i), hornblende and biotite (Fig. 3k) implying post-equilibrium crystallization from a hybrid magma (enclave milieu) and (b) quartz phenocrysts that intruded or are cross-cut by mafic minerals along their cracks or spaces generated during the mechanical transfer from the felsic melt to the mafic one (Fig. 3h, i), which clearly indicates hybridization process (e.g., Vernon, 1983). New quartz growth that primarily crystallized in the felsic melt (Fig. 2k, l) is further exhibited by the quartz and plagioclase textures in Fig. (3f). A two-step mixing model scenario (Fig. 9d) is favoured, with the first step representing mixing of two magmas of contrasting felsic and mafic compositions and crystallization of fine-grained plagioclase laths due to supercooling of the mafic system. The second step is accompanied by the development of a mesostasis-like texture in the MMEs, where the partially crystallized mafic globules from the previous step interact with felsic magma and large anhedral quartz enclose the early formed plagioclase laths (Kumar, 1995). In this case, the large quartz seems to represent a quenched hybrid system.

Progressive mingling to mixing processes, following the paths of convective currents in the magma chamber, leads to compositional hybridization by disaggregation of the MMEs, which is reflected by the

Fig. 9. Schematic illustration explaining the mechanisms by which, the magmatic deformations, and magma mixing and mingling textures in the GGC have formed and originated. (**a**) Magmatic deformations inherent in magma flow fabrics of host felsic magma, viscous finger/chaotic advection process and dynamic rotational stretching of hotter mafic magma blob during its injection into cooler felsic magma. (**b**) Mechanism of quartz ocellar formation. (**c**) K-feldspar megacyst similar to ocellar texture. (**d**) Plagioclase-quartz texture as a clear example for mixing-quench one. See text for more explanation.

schlieren trails of mafic minerals in Figs. (3i, k and 9a) (e.g., Kumar, 2010).

8.1.3. Geochemical and isotopic evidence for magma mixing/mingling

The geochemical behaviour of major and trace elements during magma mixing can be variable; the major elements can not easily diffuse and equilibrate since they represent network-forming components (mainly at tetrahedral sites) of the silicate melt, while trace elements, except Zr, and associated isotopic systems are non-network components and can easily be mobilized and diffuse more rapidly towards more homogeneous compositions after mixing (Dahlquist, 2002; Lesher, 2010).

However, mixing can be chaotic in nature and does not essentially produce linear or curvilinear trends for all the elements, but such trends of major oxides against SiO_2 on Harker variation plots (Fig. 6), indicate a possible role for mixing between mafic-felsic end-member magmas (e.g., Castro et al., 1990; Kumar and Rino, 2006; Bora et al., 2013). The widely scattered trace element patterns on Harker-style plots can also be attributed to the sorting or incorporation of key minerals including apatite and zircon or erratic elemental diffusion during synchronous magma mixing and fractionation processes (e.g., Kumar and Pieru, 2010; Kumar et al., 2017).

The higher TiO_2 (0.52–1.25 wt%) and P_2O_5 (0.15–0.41 wt%) abundance in the MMEs compared to the host monzogranites (TiO_2: 0.16–0.43 wt%) and (P_2O_5: 0.04–0.14 wt%), is attributed to the diffusion of Ti and P from the felsic magma to the MME globules during mingling, supported by the presence of titano-magnetite, titanite, and apatite in the MMEs. Zircon is a preferential inclusion in biotite, which is

abundant in the MMEs, probably due to local saturation of Zr adjacent to growing crystals (Bea, 1996), during the mixing process, which is reflected in higher Zr content of the MMEs than the host rock. However, the higher concentration of Zr in the MMEs (43.25–577.68 ppm) than the host monzogranites (71–192.4 ppm) can be in part attributed to the mixing between mantle mafic and crustal felsic magmas. It must be considered an original trait from the source region most likely through the incorporation of crustal components during magma genesis (further discussed in section 8.2), because an unmodified pristine mafic magma is not typically capable of crystallizing large amounts of zircon (Bora et al., 2013).

Other geochemical evidence in support of magma mixing process is the migration of the highly mobile elements as confirmed by the experimental results (Watson and Jurewicz, 1984; Johnston and Wyllie, 1988), where Si, Na, K, and Rb tend to migrate from felsic magma to co-existing mafic magma during mixing and supercooling/crystallization. The Na_2O enrichment in the MMEs relative to the host monzogranites is most likely related to Na migration from the felsic host to the MME,

which is consistent with albitic (Na-rich) margins of plagioclase phenocrysts/ megacrysts. However, contrary to Na_2O, the K_2O depletion in the MMEs indicate the parent magma was probably depleted in K because of early crystallization of biotite.

Uranium is preferentially concentrated in highly differentiated rocks such as granites (average; 2.9 ppm) relative to the mafic rocks (~0.5 ppm), because of its incompatibility and incorporation into accessory minerals such as zircon and monazite. The MMEs record higher U contents as compared to the monzogranites (MMEs: 1.26–13.2 ppm; monzogranites: 0.69–4.92 ppm; Table 3) and in some MMEs (8 ppm) clearly exceed typical upper crustal values. The observed enrichment in U, HFSE, and REE of the MMEs relative to their monzogranites indicates protracted residence times of the MME in the felsic host, giving an opportunity of diffusion and transfer of these elements from the monzogranitic melt into the MME, taking place probably during magma mingling/mixing. The rate of trace element and REE diffusion during magma mixing and mingling is variable, whereas the rate of LREE diffusion is higher as compared to the HREE (Baker, 1990).
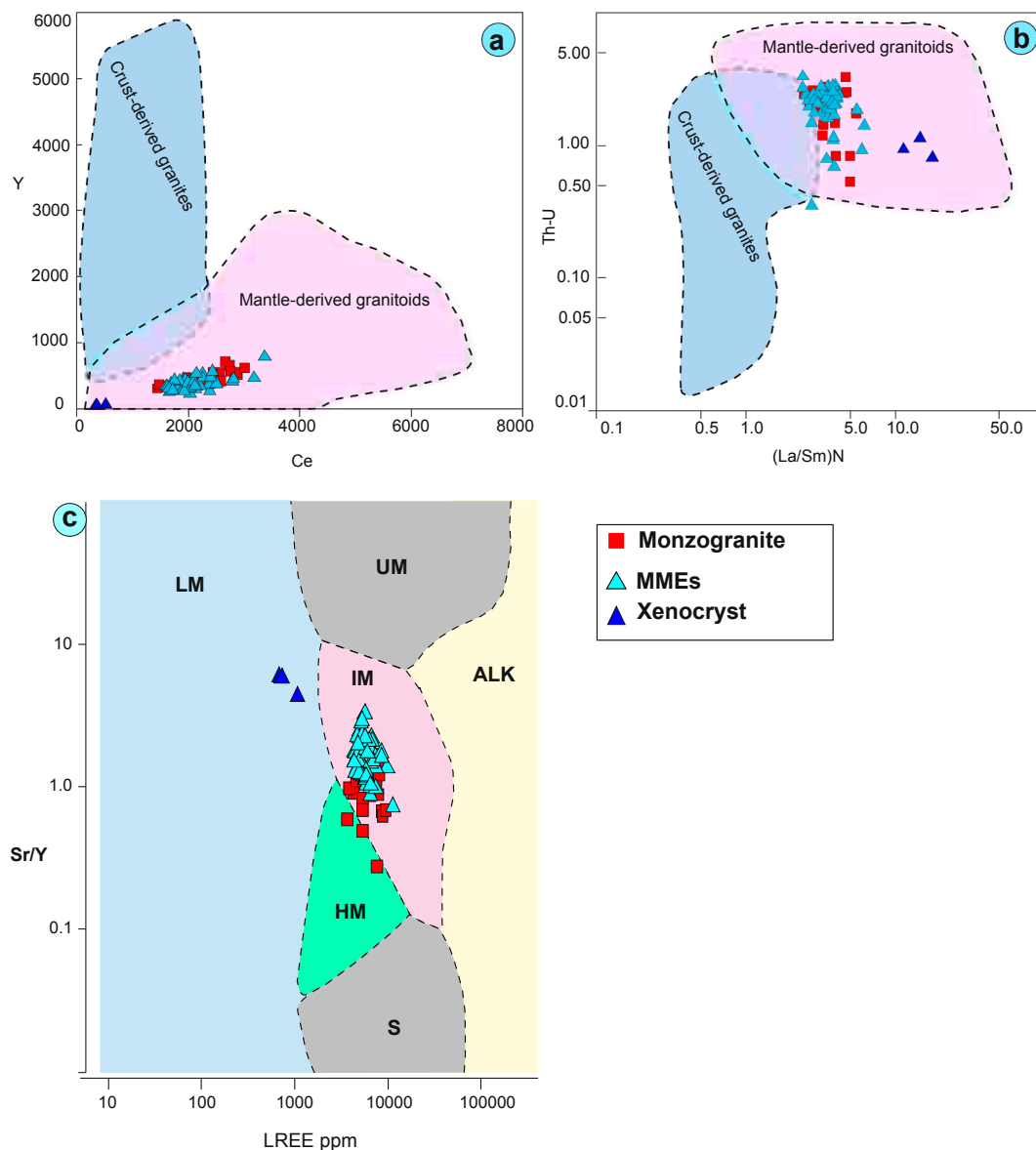
Fig. 10. Binary plots showing the origin of the BH granite (GRC101) and MME (GRC101EN); **(a)** Y vs. Ce (Laurent et al., 2017), **(b)** Th/U vs. La/Sm (Laurent et al., 2017), and **(c)** Sr/Y vs. ΣLREE (defined here as La to Nd) (O'Sullivan et al., 2020). Abbreviations for groups: ALK = alkali-rich igneous rocks; IM = mafic I-type granitoids and mafic igneous rocks; LM = low- and medium-grade metamorphic and metasomatic; HM = partial-melts/leucosomes/high-grade metamorphic; S = S-type granitoids and high aluminium saturation index (ASI) 'felsic' I-types; UM = ultramafic rocks including carbonatites, lherzolites and pyroxenites.

Although the initial Sr and Nd ratios suggest a genetic relation between the MMEs and monzogranites, the effect of isotopic equilibration during mingling/mixing process (e.g., Barbarin, 2005; Zhang et al., 2016) cannot be ignored. Likewise, the similarity and overlap in the trace element concentrations and ratios in apatites, including Ce, Y, La/Sm, and Th/U from MMEs and monzogranites (Fig. 10a, b) most likely reflect the equilibration during the interaction between two magmas (Laurent et al., 2017). The role of magma mixing/mingling and a hybrid origin for the MMEs has also been demonstrated using some geochemical plots represented on Fig. 11 (e.g., Blundy and Sparks, 1992; Zhou, 1994).

The age difference from apatite and zircon for the MME (608 and 617 Ma) and its host granite (600 and 612 Ma), is not significant in view of the analytical uncertainties. Thus, a similar zircon crystallization age of $\approx$ 610 Ma both in the MME and monzogranites reflect the coeval nature of the mafic (MME) and the felsic host magmas (monzogranite) and is consistent with mixing/mingling model.

8.2. Possible source(s) of the MMEs and the monzogranites

It has been demonstrated that two main magmatic sources of contrasting crustal and mantle compositions were involved in magma genesis. In order to model the tectono-magmatic evolution of the GGC, further investigations on the nature and composition of the source regions are required.

The crust-like major and trace element composition of the monzogranites and MMEs, wide range of SiO_2 contents (51–74 wt%), lack of typical peraluminous minerals (e.g., cordierite, andalusite, and garnet) or alkaline mafic minerals (e.g., arfvedsonite, riebeckite, and aegirine - augite), metaluminous nature and lack of upper crustal xenoliths along with low initial $^{87}Sr/^{86}Sr$ (Sr$_I$) ratios and slight bias towards adakitic-like melts (Supplementary Item-I, Fig. S5c-d) indicate possible involvement

of the lower crust in their magma genesis, similar to the monzogranites from the Gattar batholith, NED (El-Sayed et al., 2003; Mahdy et al., 2015).

The zircon U-Pb age data together with low Sr$_I$ ratios and positive $\varepsilon Nd_{(t)}$ values indicates the incorporation of the ANS juvenile crust in magma genesis, such as the *ca.* 762–723 Ma pre Pan-African crust of the Eastern Desert of Egypt (Dixon and Golombek, 1988). Liégeois and Stern (2010) reported similar initial $^{87}Sr/^{86}Sr$ ratios (0.70252) and positive $\varepsilon Nd^{(t)}$ values (+6.4) for the Meatiq and Hafafit gneisses, which precludes contribution of pre-Neoproterozoic crust in the Eastern Desert. Similarly, the positive $\varepsilon Nd^{(t)}$ values (+1.5 to + 8.9) for the northern ANS (Johnson, 2014) support a juvenile magmatic event. In addition, the low δEu (Eu/Eu* or Eu anomaly) (MMEs: 0.30–1.00; *av.* 0.47 and monzogranites: 0.27–0.61; *av.* 0.39), and fairly high δCe (Ce anomaly) (MMEs: 1.01–1.11; *av.* 1.05 and monzogranites: 1.00–1.20; *av.* 1.08) values of the apatites as well as similar La/Sm (monzogranite: *av.* 5.9 ppm; MME: *av.* 5.7, except three high values of 18–28) and variable Sr/Th in apatites (monzogranite: 4.35–36.89 ppm; MME: 13.08–108.1 ppm) indicate the volatile/fluids released from remnants of dehydrated oceanic slab played a key role for partial melting of juvenile crustal material (Zhu et al., 2009; Zafar et al., 2020).

However, the noticeably low Cr (monzogranites: 0.4–19 ppm; MMEs: 0.4–179 ppm) and Ni (monzogranites: 5.7–14 ppm; MMEs: 1.9–68 ppm) and Rb/Sr (0.06–0.40) of the monzogranites do not correlate with those of the mantle (Rb/Sr ratio; 0.01–0.10; Taylor and McLennan, 1985, 1995; Hofmann, 1988), the medium- to high-K calc-alkaline affinity, the LILE (Rb, Sr, Ba, and K) enrichment over HFSE (Y, Nb, Ta, Zr, and Hf), the negative Nb, Ti, and P anomalies, collectively indicate the involvement of a lithospheric mantle component in their magma genesis. The low Nb/La ratios ($\leq$0.5) on Nb/La *vs* La/Yb plot (Fig. 12) also support the contribution of the lithospheric mantle source (e.g., Abdel-Rahman and Nassar, 2004). It is consistent with high Sr/Th ratios of apatites,
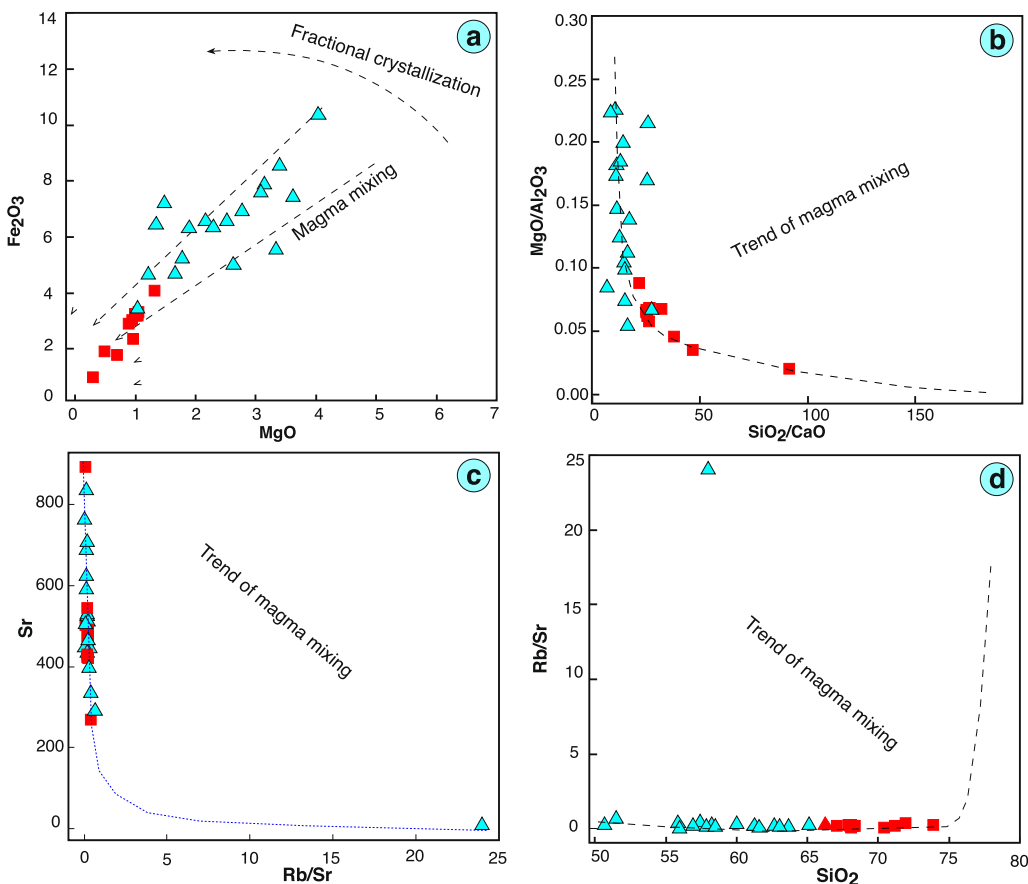
Fig. 11. Some chemical plots supporting the crystal-charged magma mixing/mingling model. Plots of (**a**) Fe$_2$O$_3$ *vs.* MgO, (**b**) MgO/Al$_2$O$_3$ *vs.* SiO$_2$/CaO, (**c**) Sr *vs.* Rh/Sr, (**d**) Rb/Sr *vs.* SiO$_2$ delineated by Blundy and Sparks (1992), Zorpi et al. (1989), and Zhou (1994) who defined trends resembling with those of rocks to have a hybrid origin, which favored a magma mixing/mingling model for the MMEs of Gharib complex. Plots of (**e**) SiO$_2$ *vs.* ε_{Nd} (t) and (**f**) SiO$_2$ *vs.* initial $^{87}Sr/^{86}Sr$ clarifying the role of diffusive fractionation in the evolution of the MMEs and monzogranites in Gharib complex.
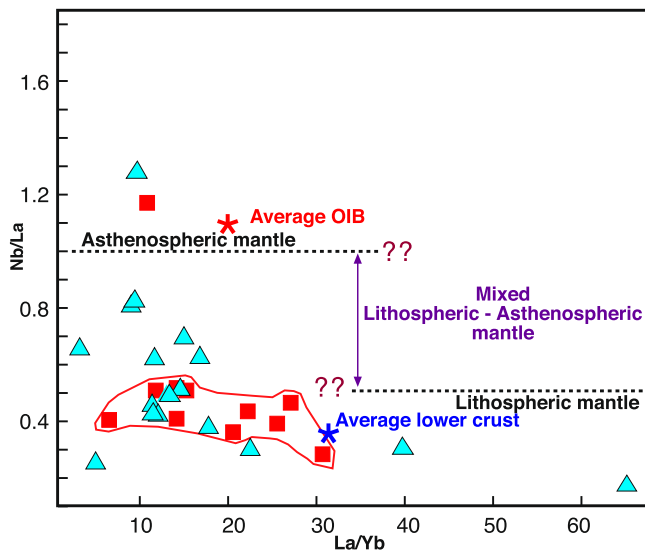
Fig. 12. Nb/La vs. La/Yb plot suggested by (Abdel-Rahman and Nassar, 2004) to differentiate between magmas derived from lithospheric mantle and asthenospheric mantle for the MMEs and host BH granites.

especially in MMEs, where melting of lithospheric mantle stimulated through slab-derived fluids favourably concentrates Sr and Th (Turner and Foden, 2001; Labanieh et al., 2012).

The clear positive εNd values and low initial $^{87}Sr/^{86}Sr$ ratios for the MMEs (+3.45 - +5.49 and 0.703015 - 0.703729) and for the monzogranites (+2.29 - +4.57 and 0.703062 - 0.704066), respectively, indicate that the lithospheric mantle source was isotopically depleted. It is further supported by the apatite chemistry data (Supplementary Item-III, Table S6), where the samples plotted in the field of I-type mafic magma (IM-type) field on the $\sum$LREE vs. Sr/Y diagram (Fig. 10c) of O'Sullivan et al. (2020). All evidences indicate a mixed crustal-mantle scenario in which the lithospheric mantle melt has been hybridized with crustal melts.

The high modal abundance of hornblende and biotite in the monzogranites and the MMEs indicates the assumed parent magmas are water and volatile (especially fluorine) saturated (e.g., Richard et al., 2006; Feig et al., 2010), which is consistent with the preservation of the subduction components (fluids/melts) long after collision and complete slab removal from the source region. The high Ce^{3+}/Ce^{4+} and Eu^{2+}/Eu^{3+} ratios, as well as lower Eu^{3+} concentrations ratios in magma, resulting in positive Ce and robust negative δEu in apatite, demonstrate low oxygen fugacity (fO_2) conditions (Cao et al., 2012), consistent with negative Eu-anomaly in whole-rock composition of MMEs and monzogranites. Magma differentiation at low $f(O_2)$ excludes early fractionation of Fe–Ti-oxides, which is reflected in crystallization of ilmenite in these rocks.

9. Modelling the genesis and evolution of the MMEs and host monzogranites

As discussed earlier, the preferential transfer of minerals from host magma to the hybrid zone (parent for MMEs) modifies the chemistry of the MMEs, thus a composition closer to the original traits can be achieved by subtracting the transferred crystal cargo from the hybrid zone. Based on petrographic evidence, quartz, plagioclase, and K-feldspar phenocrysts are the main minerals that underwent transfer in addition to apatites. Quartz transfer was the main influence on the whole-rock SiO_2 content, thus, the classification of MMEs, where the more mafic MMEs (SiO_2: 51–56 wt%) exhibit higher REE concentrations than those of intermediate ones (SiO_2: 57–66 wt%). This signature along with similar $Mg^{\#}$ (0.19–0.31 and 0.22–0.4) and Sr-Nd isotopic ratios support the idea
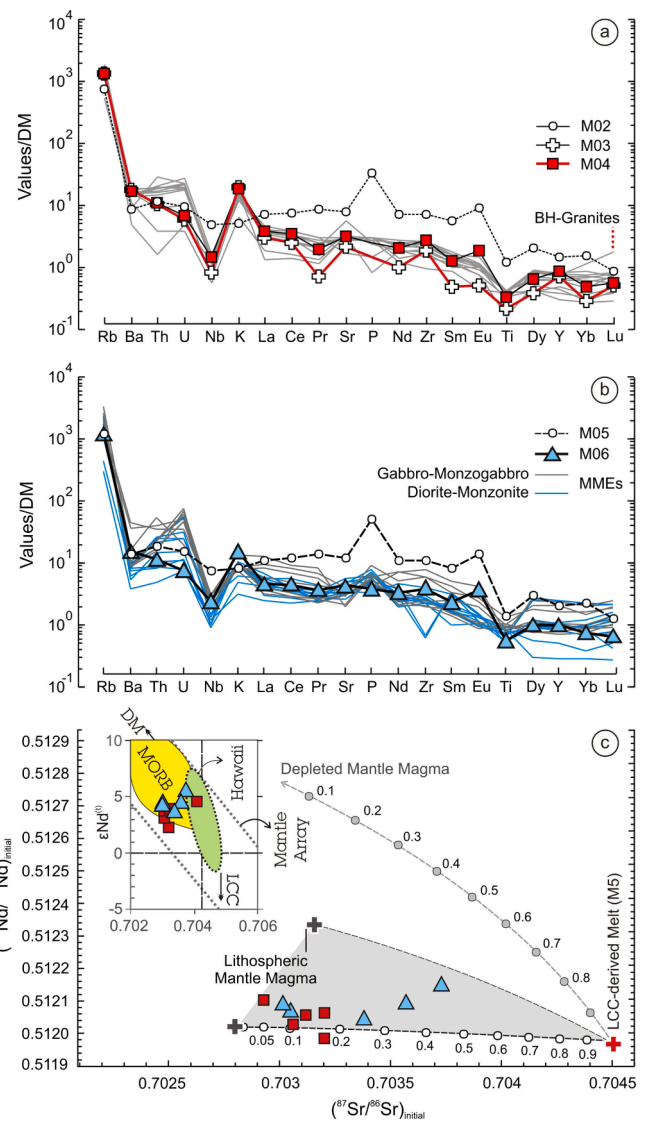

Fig. 13. Multielement models of melting and mixing processes for the formation of **(a)** host monzogranites (M4), and **(b)** MMEs (M6) and **(c)** Binary mixing model on $^{144}Nd/^{143}Nd$ vs. $^{87}Sr/^{86}Sr$ plot, explaining the isotopically depleted nature of the monzogranites and their associated MMEs. The inset εNd vs. $^{87}Sr/^{86}Sr$ plot shows an affinity to MORB-like depleted mantle source for these samples. The results and parameters used for the calculations are given in Supplementary Items-III, Tables S7, S8, and S9. The normalizing values (DM) is from Workman and Hart (2005).

that the intermediate MMEs and the felsic ones (i.e., GRC-21EN used for age dating) are originally mafic and intermediate in composition, respectively, and were affected by transfer of quartz crystals from the host felsic magma.

The plagioclase shows the highest compositional overlap between the MME and the monzogranites (Fig. 4a-c). Considering the trace element partition coefficient between minerals and felsic magma, feldspars can have the greatest impact on Sr and Eu values, and apatite on the MREE plus U concentrations (Supplementary Item-III, Table S7). However, the composition of the hybrid magma shows that the low modal abundances of the transferred minerals (apatites < 1 vol%; plagioclase and K-feldspar < 5 vol%), did not significantly modify the bulk-rock trace element composition (as shown for apatites in Supplementary Item-I, Fig. S8). Mineral transfer along with geochemical and isotopic equilibration between the monzogranites and their MMEs suggest that system has been closed after magma mixing/mingling events
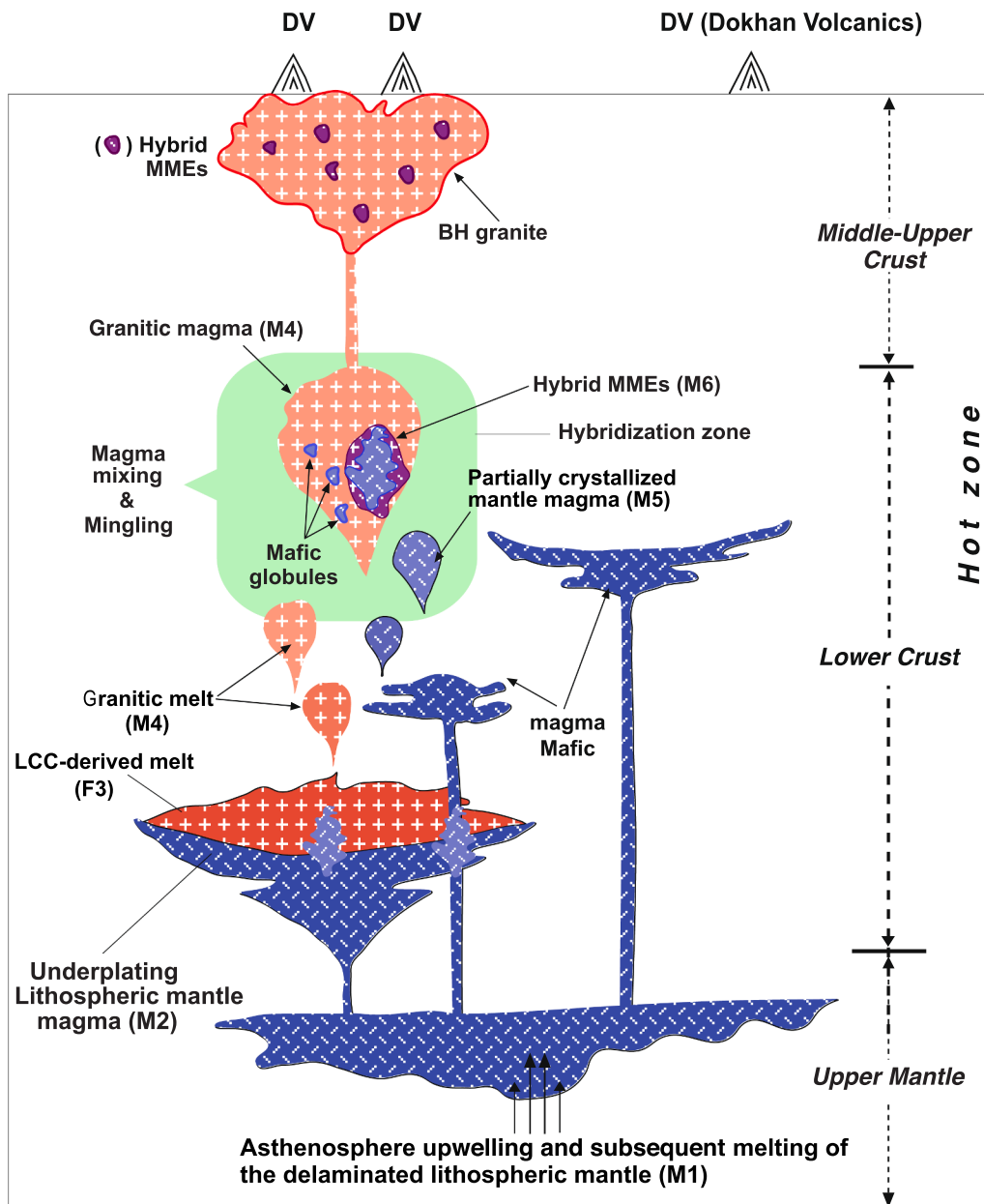
Fig. 14. Sketch model of the monzogranites and their hybrid to MMEs genesis and evolution.

until final crystallization.

The contribution of the mafic end-member in the hybrid magma, originated from the lithospheric mantle source, can also be explained within the tectono-magmatic framework of the study area. Widespread late-orogenic calc–alkaline magmatism shifted to extensional alkaline activity in the ANS at 630–590 Ma was accompanied by rapid and intensive erosional denudation and Late Neoproterozoic crustal thickening followed by lithospheric mantle removal/delamination (e.g., Avigad and Gvirtzman, 2009). The removal/delamination process and erosional decompression can potentially remove dense ultramafic cumulates and garnet granulites from the lower continental crust and cause upwelling of hot asthenosphere thereby triggering partial melting of the overlying ANS residual lithospheric mantle and lower crust. The geochemical evidence confirms the role of long-lived volatiles and fluids released from detached oceanic crust in the melting of the sub-lithosphere mantle and lower crust.

Pristine basaltic magma derived from lithospheric mantle (M1, F_{mel}: 0.15; melting model parameters in Supplementary Item-III, Table S8),

raised, underplated, pooled, and experienced some extent of fractionation in contact with cold lower crust (M2: partially crystallized mafic magma, F_c: 0.05). The heat transferred from partially crystallized mantle magma, melted the juvenile mafic lower crust (M3, F_{mel}: 0.1), and subsequent interaction between them produced a metaluminous felsic magma as a parent for the monzogranites (M4, F_{mix}: 0.1; Table 5, Fig. 13a, Fig. 14). The injection of new pulses of partially crystallized mantle magma (M5, F_c: 0.08) into felsic magmas (i.e., M4) in a deep crust hot zone developed a hybrid magma zone in the contact area between them which enclosed hybrid MMEs (M6, F_{mix}: 0.25; Table 5, Fig. 13b, Fig. 14), and mafic globules. The irregular plateau and zones of anorthite formed in the plagioclase phenocrysts transferred from the host felsic magma to the MMEs demonstrate the higher temperature and relatively more mafic nature of the hybrid zone compared to the felsic magma. It is inferred that the water content of the melt lowered the density difference between the felsic and mafic magmas, facilitating thus mixing and triggering crystal transfer.

According to the trace element modelling, the lithospheric mantle

Table 5

The results of melting and mixing and fractional crystallization model calculations.

	Hot Zone								En route	
	Upper Mantle				Lower Crust					
		Melting	FC*3		Melting			Mixing	FC*4	Mixing
	PM*1	M1	D1	M2	LCC*2	D2	M3	M4	M5	M6
		F_{mel} 0.15	0.00	$F_c = 0.05$			$F_{mel} = 0.1$	$F_{mix} = 0.10$	$F_c = 0.08$	$F_{mix} = 0.25$
Rb	0.63	3.60	0.02	71.84	24	0.20	79.11	78.38	44.91	70.01
Ba	6.99	41.22	0.00	786.96	388	0.30	1000.82	979.44	495.45	858.44
Th	0.09	0.56	0.00	11.07	1.64	0.12	6.28	6.76	6.93	6.80
U	0.02	0.14	0.13	2.73	1.50	0.03	1.05	1.22	1.71	1.34
Nb	0.71	4.52	0.01	61.74	7.75*	1.13	6.95	12.43	40.96	19.56
K	249.98	881.81	0.03	17090.66	11,050	0.14	41630.87	39176.85	10734.45	32066.25
La	0.69	3.82	0.04	69.36	21.60	1.17	18.78	23.84	44.01	28.88
Ce	1.77	10.18	0.01	178.79	46.40*	1.27	37.49	51.62	114.05	67.23
Pr	0.28	1.47	0.05	28.02	3.40*	2.51	1.44	4.10	17.63	7.48
Sr	21.10	109.90	0.03	1887.73	495	1.50	342.86	497.35	1208.34	675.10
P	94.98	582.43	0.08	10748.35	3317.1*	–	–	–	6803.03	–
Nd	1.35	6.53	0.09	101.24	23.50	2.86	8.81	18.05	65.85	30.00
Zr	11.20	52.36	0.15	806.97	47	0.25	136.99	203.99	525.41	284.35
Sm	0.44	1.67	0.04	21.58	5	4.24	1.28	3.31	14.45	6.09
Eu	0.17	0.74	0.74	13.01	1.80*	4.13	0.47	1.73	8.30	3.37
Ti	1300.24	3839.46	0.21	8374.91	5755	4.92	1273.41	1983.56	7410.36	3340.26
Dy	0.74	1.00	0.32	10.57	7.80*	6.33	1.35	2.27	7.30	3.53
Y	4.55	5.79	0.16	45.05	28	1.88	15.69	18.62	32.66	22.13
Yb	0.49	0.44	0.21	5.39	3.10	4.94	0.68	1.15	3.64	1.77
Lu	0.07	0.04	0.00	0.44	0.70*	4.24	0.18	0.20	0.30	0.23

*1 Primitive mantle composition (Sun and McDonough, 1989)

*2 Lower continental crust amphibolite composition (Tatsumi, 2000; *Qian and Hermann, 2013).

*3, *4 Fractional crystallization of lithospheric mantle magma (using D1)

M1: Melting of delaminated subcontinental lithospheric mantle (non-modal batch melting of amphibole-bearing garnet-spinel lherzolite).

M2: Partial crystallization of depleted mantle magma (M4) at the bottom of the continental crust.

M3: LCC-derived melt (modal Fractional Melting of amphibolitic lower crust).

M4: Parent magma for BH granites.

M5: Partial crystallization of depleted mantle magma at en route to the surface.

M6: Mixing between M4 and crystal-charged M5 magma form the hybrid parent magma for MMEs

M6: M4 magma composition after fractional crystallization.

Abbreviations: Degree of melting (F_{mel}), fractional crystallization (F_c), and mixing (F_{mix}).

D1: for Olv (0.6) + Cpx (0.4).

D2: for Am (0.7) + Plg (0.3).

Partition coefficient for each element in these minerals is given in Supplementary Item-III, Table S7.

Melting parameters have been given in Supplementary Item-III, Table S8.

Mixing equation is from Langmuir et al. (1978).

*3 MMEs: Mafic Microgranular Enclaves.

magma has been involved in higher proportion into hybrid MME magmas (M6, F_{mix}: 0.25) compared to the felsic parent ones (M4, F_{mix}: 0.1). This is consistent with the higher Sr/Th ratios of apatites from the MMEs than the monzogranites.

The binary isotope mixing model (Fig. 13c, Supplementary Item-III, Table S9) also confirms the incorporation of the lower crust in magma genesis and the interaction between the lower crust-derived melt and depleted mantle magma within a crustal hot zone, which explains the depleted signature of the monzogranites and their associated MMEs. The similar isotopic composition of monzogranites and MMEs, however, can be taken as evidence for the isotopic exchange and homogenization, once these magmas come into physical contact, similar to that of observed by Sarjoughian et al. (2019), Poli et al (2020) and Barnes et al. (2021).

The magmatic assemblages, comprising metaluminous I-type felsic magma, mafic globules and associated crystal-charged hybrid MME, were forcibly injected into shallow crustal chambers through feeder dykes. This is reflected in sieve-like and patchy zoned textures in plagioclase from the monzogranites. These textures also indicate the changes in temperature and composition of the host magma (Castro, 2001) during mafic-felsic magma mixing. Partial dissolution of some interstitial quartz and K-feldspar crystals and the development of the ocellar texture in MMEs indicate the influence of turbulent convection in the feeder channels.

This scenario appears similar to the magma mixing plus fractional crystallization (MFC ± crustal assimilation) model of Poli et al. (2020), especially in terms of magma generation in the source region and subsequent magma mixing process, but gives more weight to the magma mixing and transfer of felsic minerals from the felsic melt to the hybridization zone, and supercooling/quenching process and disequilibrium growth rather than progressive magmatic fractionation and crustal assimilation. The geochemical and isotopic evidences include higher REE concentrations in the mafic MMEs compared to the host monzogranites and low ($^{87}Sr/^{86}Sr$)$_{initial}$ in the MMEs and host monzogranites and argues against magmatic fractionation and upper crustal involvement in the magma genesis.

10. Conclusions

The monzogranites, the dominant granite variety in the GGC of the NED, contain abundant MMEs. The MMEs exhibit porphyritic and poikilitic textures and are finer grained and darker than their equigranular host monzogranites. They noticeably show greater abundances of mafic minerals, i.e., hornblende and biotite, than their host monzogranites.

The linear to curvilinear chemical variations of the MMEs and the monzogranites on Harker diagrams and the Sr-Nd isotopic data suggest that magma mixing was the main process in their genesis and evolution. This is supported by micro-textural and mineral-chemical features and

strongly argues against other models for the genesis of the MMEs.

The existence of chilled margins and fragments of the monzogranites in the MMEs in outcrop along with textural evidence supporting the mechanical transfer of minerals crystallized in felsic magma to the mafic melt (e.g., feldspar phenocrysts cross-cutting the MME–host boundaries, stubby apatite, quartz ocelli and poikilitic outermost rims of K-feldspar phenocrysts), supercooling/quenching process (e.g., acicular apatite and elongated hornblende and biotite crystals), and disequilibrium growth (e.g., hornblende-biotite clots replaced early crystallized clinopyroxene) favours a magma mingling/mixing process in their genesis. It is supported by geochemical and isotopic data suggesting the MMEs as supercooled hybrid globules within a cooler, partially crystallized host felsic magma.

The geochemical evidence including crust-like major and trace element compositions of the monzogranites and MMEs, the wide range of SiO_2 contents, lack of typical peraluminous minerals or alkaline mafic minerals, metaluminous nature and lack of upper crustal xenoliths along with a slight bias towards adakitic-like melts suggest the possible involvement of the lower crust in magma genesis. The zircon and apatite age data together with low Sr_I ratios and positive $\varepsilon_{Nd(t)}$ values indicate the incorporation of the ANS juvenile crust in magma genesis. The medium- to high-K calc-alkaline affinity, the LILE enrichment, the negative Nb, Ti, and P anomalies, and low Nb/La ratios, collectively indicate the contribution of a lithospheric mantle source in magma genesis. The low δEu and fairly high δCe values as well as the similar La/Sm and variable Sr/Th in apatites of the monzogranites and MMEs indicate the contribution of volatile/fluids from the remnants of the oceanic slab in triggering the melting of lithospheric mantle and juvenile crust.

Integration of field, petrographic, geochemical, and Sr-Nd isotopic data with U-Pb zircon and apatite ages, a two-step process is suggested for the evolution of the MMEs and monzogranites. The first step involves partial melting of depleted lithospheric mantle ($F_{mel} \sim 0.15$) due to asthenosphere upwelling after removal of a delaminated lithospheric root and dense lower crust, facilitated by the long-lived fluids released from the remnants of the oceanic slab. It is followed by melting of the juvenile mafic lower crust by underplated depleted lithospheric mantle magma. The interaction between LCC-derived melt and partially crystallized mantle magma produced the I-type metaluminous parent magma for the monzogranites ($F_{mix} \sim 0.1$). The intrusion of new pulses of crystal-charged mantle magma into granitic magma and subsequent magma mixing/mingling generated a hybridization zone that contain hybrid MMEs ($F_{mix} \sim 0.25$).

There was thus a complex post-collisional interplay between asthenosphere, lithospheric mantle, and lower crust, triggered by the removal of delaminated lithospheric root and slab break-off due to collision of East and West Gondwana during the final stage of the ANS evolution in the Neoproterozoic, to produce the post-orogenic monzogranites and their MMEs.

Credit Author Statement

H.A. Eliwa devised the project, the main conceptual ideas and proof outline. H.A. Eliwa analyzed and interpreted the analytical data and wrote the manuscript in consultation with N.M. Mahdy, R. Deevsalar, and S. Kumar. D. Chew and A. Anderson carried out the compositional analysis and U-Pb dating of apatite and zircon, respectively, as well as supervising, discussing and revising the findings of this work. H.A. Eliwa, M. Murata, H. Ozawa assisted in the measurements of whole rock and mineral analyses. Y. Kato and K. Fujinaga analyzed the whole rock and rare earth elements. I.M. Khalaf, A. Afandy, and Kh. El Gameel assisted in field work, designed the figures, and contributed to the interpretation of the results. Z. Tehseen assisted in writing and interpreting the apatite composition section. M. Fawzy separated zircons and apatite. All authors discussed the results, provided critical feedback and contributed to the final manuscript shape.

Appendix A. Supplementary data

Supplementary data to this article can be found online at https://doi.org/10.1016/j.precamres.2021.106380.

References

Abdel-Rahman, A.F.M., 1994. Nature of biotites from alkaline, calc-alkaline, and peraluminous magmas. J. Petrol. 35, 525–541.

Abdel-Rahman, A.F.M., 1995. Tectonic-magmatic stages of shield evolution: The Pan-African belt in northeastern Egypt. Tectonophysics 242, 223–240.

Abdel-Rahman, A.F.M., Nassar, P.E., 2004. Cenozoic Volcanism in the Middle East: Petrogenesis of alkali basalts from Northern Lebanon. Geol. Mag. 141, 545–563.

Abdel-Rahman, A.M., Martin, R.F., 1990. The Mount Gharib A-type granite, Nubian Shield: petrogenesis and role of metasomatism at the source. Contrib. Miner. Petrol. 104, 173–183.

Adam, M.S.M., Kim, T., Song, Y.S., Kim, Y.S., 2019. Occurrence and origin of the zoned microgranular enclaves (MEs) within the Cretaceous granite in Taejongdae, SE Korea. Lithos 324–325, 537–550.

Avigad, D., Gvirtzman, Z., 2009. Late Neoproterozoic rise and fall of the northern Arabian-Nubian Shield: The role of lithospheric mantle delamination and subsequent thermal subsidence. Tectonophysics 477, 217–228.

Baker, D.R., 1990. Chemical inter-diffusion of dacite and rhyolite: anhydrous measurements at 1 atm and 10 kbar, application of transition state theory, and diffusion in zoned magma chambers. Contrib. Miner. Petrol. 104, 407–423.

Barbarin, B., 2005. Mafic magmatic enclaves and mafic rocks associated with some granitoids of the central Sierra Nevada batholith, California: nature, origin, and relations with the hosts. Lithos 80, 155–177.

Barnes, C.G., Werts, K., Memeti, V., Paterson, S.R., Bremer, R., 2021. A tale of five enclaves: Mineral perspectives on origins of mafic enclaves in the Tuolumne Intrusive Complex. Geosphere 17, 352–374.

Bateman, R., 1995. The interplay between crystallization, replenishment and hybridization in large felsic magma chambers. Earth-Sci. Rev. 39 (1–2), 91–106.

Baxter, S., Feely, M., 2002. Magma mixing and mingling in granitoids: examples from the Galway Granite, Connemara, Ireland. Mineral. Petrol. 76, 63–74.

Bea, F., 1996. Controls on the trace element composition of crustal melts. Trans. Roy. Soc. Edinburgh: Earth Sci. 87, 33–41.

Bennett, E.N., Lissenberg, C.J., Cashman, K.V., 2019. The significance of plagioclase textures in mid-ocean ridge basalt (Gakkel Ridge, Arctic Ocean). Contrib. Miner. Petrol. 174 (49), 1–22.

Blundy, J.D., Sparks, R.S.J., 1992. Petrogenesis of mafic inclusions in granitoids of the Andamello Massif, Italy. J. Petrol. 33 (5), 1039.

Bora, S., Kumar, S., Yi, K., Namhoon, K., Lee, T.H., 2013. Geochemistry and U-Pb SHRIMP Zircon chronology of granitoids and microgranular enclaves from Jhirgadandi pluton of Mahakoshal belt, Central India Tectonic Zone, India. J. Asian Earth Sci. 70–71, 99–114.

Cao, M., Li, G., Qin, K., Seitmuratova, E.Y., Liu, Y., 2012. Major and trace element characteristics of apatites in granitoids from Central Kazakhstan: implications for petrogenesis and mineralization. Resour. Geol. 62, 63–83.

Castro, A., 1990. Microgranular enclaves of the Quintana granodiorite (Los Pedroches batholith). Petrogenetic significance. Rev. Soc. Geol. España 3, 7–21.

Castro, A., 2001. Plagioclase morphologies in assimilation experiments. Implications for disequilibrium melting in the generation of granodiorite rocks. Mineral. Petrol. 71, 31–49.

Castro, A., Rosa, J.D., Stephens, W.E., 1990. Magma mixing in the subvolcanic environment: petrology of the Gerena interaction zone near Seville, Spain. Contrib. Miner. Petrol. 105, 9–26.

Chappell, B.W., White, A.J.R., Wyborn, D., 1987. The importance of residual source material (restite) in granite petrogenesis. J. Petrol. 28, 1111–1138.

Chappell, B.W., White, A.J.R., 1992. I- and S-type granites in the Lachlan Fold Belt. Trans. Roy. Soc. Edinburgh Earth Sci. 83, 1–26.

Chen, Y.D., Price, R.C., White, A.J.R., 1989. Inclusions in three S-type granites from southeastern Australia. J. Petrol. 30 (1), 18.

Choe, W.H., Jwa, Y.J., 2004. Petrological and geochemical evidences for magma mixing in the Palgongsan Pluton. Geosci. J. 8 (4), 343–354.

Collins, W.J., 1998. Evaluation of petrogenetic models for Lachlan Fold Belt granitoids: implications for crustal architecture and tectonic models. Austral. J. Earth Sci. 45, 483–500.

Conard, W.K., Nicholls, I.A., Wall, V.J., 1988. Water-saturated and -undersaturated melting of metaluminous and peraluminous crustal compositions at 10 kb: Evidence for the origin of silicic magmas in the Taupo volcanic zone, New Zealand, and other occurrence. J. Petrol. 29, 765–803.

Cox, K.G., Bell, J.D., Pankhurst, R.J., 1979. The Interpretation of Igneous Rocks. George Allen and Unwin, London, p. 450.

Dahlquist, J.A., 2002. Mafic microgranular enclaves: early segregation from metaluminous magma (Sierra de Chepes), Pampean Ranges, NW Argentina. J. South Am. Earth Sci. 15, 643–655.

De Campos, C.P., Perugini, D., Ertel-Ingrisch, W., Dingwell, D.B., Poli, G., 2011. Enhancement of Magma mixing efficiency by Chaotic Dynamics: an experimental study. Contrib. Miner. Petrol. 161, 863–881.

De Campos, C.P., Perugini, D., Dingwell, D.B., Civetta, L., Fehr, T.K., 2008. Heterogeneities in Magma Chambers: insights from the behaviour of major and minor elements during mixing experiments with natural alkaline melts. Chem. Geol. 256, 131–145.

Deer, W.A., Howie, R.A., Zussman, J., 1966. An Introduction to the Rock Forming Minerals. Longman Group UK Ltd, Harlow, Essex, p. 668.

DePaolo, D.J., 1981. Neodymium isotopes in the Colorado Front Range and crust-mantle evolution in the Proterozoic. Nature 291, 193–196.

Didier, J.D., 1973. Granites and their Enclaves. Developments in Petrology 3. Elsevier, Amsterdam, p. 393.

Dixon, T.H., Golombek, M.P., 1988. Late Precambrian crustal accretion rates in Northeast Africa and Arabia. Geology 16, 991–994.

Dodge, F.C.W., Kistler, R.W., 1990. Some additional observations on inclusions in the granitic rocks of the Sierra Nevada. J. Geophys. Res. 95, 17841–17848.

Donaire, T., Pascual, E., Pin, C., Duthou, J.L., 2005. Microgranular enclaves as evidence of rapid cooling in granitoid rocks: the case of the Los Pedroches granodiorite, Iberian Massif, Spain. Contrib. Miner. Petrol. 149, 247–265.

Dou, J., Huang, X., Chen, F., 2021. Successive magma mixing in deep-seated magma chambers recorded in zircon from mafic microgranular enclaves in the Triassic Mishuling granitic pluton, Western Qinling, Central China. J. Asian Earth Sci. 207, 104656.

Eliwa, H.A., Breitkreuz, C., Murata, M., Khalaf, I.M., Bühler, B., Itaya, T., Takahashi, T., Hirahara, Y., Miyazaki, T., Kimura, J.-I., Shibata, T., Koshi, Y., Kato, Y., Ozawa, H., Daas, M.A., El Gameel, Kh., 2014. SIMS zircon U-Pb and mica K-Ar geochronology, and Sr-Nd isotope geochemistry of Neoproterozoic granitoids and their bearing on the evolution of the north Eastern Desert, Egypt. Gondwana Res. 25, 1570–1598.

El-Bialy, M., Eliwa, H.A., Murata, M., Mourad, N.M., El-Gameel, K.h., Sehsah, H., Omar, M., Kato, Y., Fujinaga, K., Andresen, A., Thomsen, T.B., 2020. U-Pb zircon geochronology and geochemical constraints on the Ediacaran continental arc and post-collision Granites of Wadi Hawashiya, North Eastern Desert, Egypt: Insights into the ~600 Ma crust-forming Event in the northernmost part of Arabian-Nubian Shield. Precambr. Res. 345, 1–38.

El-Mansi, M.M., Dardier, A.M., Moussa, E.M., 2004. Geology and uranium distribution within the older granitoids and some granitic masses in the North Eastern Desert, Egypt. Egypt. J. Geol. 48, 101–114.

El-Sayed, M.M., Shalaby, M.H., Hassanen, M.A., 2003. Petrological and geochemical constraints on the tectonomagmatic evolution of the late Neoproterozoic granitoid suites in the Gattar area, North Eastern Desert, Egypt. Neues Jahrbuch für Mineralogie - Abhandlungen 178 (3), 239–275.

Eyal, M., Litvinovsky, B., Jahn, B.M., Zanvilevich, A., Katzir, Y., 2010. Origin and evolution of post-collisional magmatism: coeval Neoproterozoic calc-alkaline and alkaline suites of the Sinai Peninsula. Chem. Geol. 269, 153–179.

Feig, S.T., Koepke, J., Snow, J.E., 2010. Effect of oxygen fugacity and water on phase equilibria of a hydrous tholeiitic basalt. Contrib. Miner. Petrol. 160, 551–568.

Fernández, C., Castro, A., 2018. Mechanical and structural consequences of magma differentiation at ascent conduits: a possible origin for some mafic microgranular enclaves in granites. Lithos 320–321, 49–61.

Fritz, H., Abdelsalam, M., Ali, K., Bingen, B., Collins, A.S., Fowler, A.R., Ghebreab, W., Hauzenberger, C.A., Johnson, P., Kusky, T., Macey, P., Muhongo, S., Stern, R.J., Viola, G., 2013. Orogen styles in the East African Orogens: a review of the Neoproterozoic to Cambrian tectonic evolution. J. Afr. Earth Sc. 86, 65–106.

Frost, R., Barnes, C.G., Collins, W.J., OLLINS, Arculus, R.J., David, J.E., Frost, C.D., 2001. A Geochemical Classification for Granitic Rocks. J. Petrol. 42, 2033–2048.

Garfunkel, Z., 2015. The relations between Gondwana and the adjacent peripheral Cadomian domain - constrains on the origin, history, and paleogeography of the peripheral domain. Gondwana Res. 28, 1257–1281.

Goldstein, S.L., O'Nions, R.K., Hamilton, P.J., 1984. A Sm-Nd isotopic study of atmospheric dusts and particulates from major river systems. Earth Planet. Sci. Lett. 70, 221–236.

Hargrove, U.S., Stern, R.J., Kimura, J.I., Manton, W.I., Johnson, P.R., 2006. How juvenile is the Arabian-Nubian Shield? Evidence from Nd isotopes and pre-Neoproterozoic inherited zircon in the Bi'r Umq suture zone, Saudi Arabia. Earth Planet. Sci. Lett. 252, 308–326.

Henry, D.J., Guidotti, C.V., Thomson, J.A., 2005. The Ti-saturation surface for low-to medium pressure metapelitic biotites: implications for geothermometry and Ti substitution mechanisms. Am. Mineral. 90, 316–328.

Hibbard, M.J., 1981. The magma mixing origin of mantled feldspars. Contrib. Miner. Petrol. 76, 158–170.

Hibbard, M.J., 1991. Textural anatomy of twelve magma-mixed granitoid systems. In: Didier, J., Barbarin, B. (Eds.), Enclaves and Granite Petrology, Developments in Petrology 13. Elsevier, Amsterdam, pp. 431–444.

Hibbard, M.J., 1995. Petrography to petrogenesis. Prentice Hall, New Jersey.

Hofmann, A.W., 1988. Chemical differentiation of the Earth: the relationship between mantle, continental crust and oceanic crust. Earth Planet. Sci. Lett. 90, 297–314.

Johnson, P.R., 2014. An Expanding Arabian-Nubian Shield Geochronologic and Isotopic Dataset: Defining Limits and Confirming the Tectonic Setting of a Neoproterozoic Accretionary Orogen. Open Geol. J. 8, 3–33.

Johnson, P.R., Andresen, A., Collins, A.S., Fowler, A.R., Fritz, H., Ghebreab, W., Kusky, T., Stern, R.J., 2011. Late Cryogenian-Ediacaran history of the Arabian-Nubian Shield: a review of depositional, plutonic, structural, and tectonic events in the closing stages of the northern East African Orogen. J. Afr. Earth Sc. 61, 167–232.

Johnston, A.D., Wyllie, P.J., 1988. Interaction of granitic and basaltic magmas: Experimental observations on contamination processes at 10 kbar with H2O. Contrib. Miner. Petrol. 98, 352–362.

Kumar, S., 1995. Microstructural evidence of magma quenching inferred from enclaves hosted in the Hodrusa granodiorites, Western Carpathians. Geol. Carpath. 46, 379–382.

Kumar, S., 2010. Mafic to hybrid microgranular enclaves in the granitoids of Ladakh batholith, Northwest Higher Himalaya: implications on calc-alkaline magma chamber processes. J. Geol. Soc. India 76, 1–25.

Kumar, S., Kumar, S., 2014. Magmatic Processes: Review of Some Concepts and Models. In Modelling of Magmatic and Allied Processes. Springer-Switzerland, pp. 1–22.

Kumar, S., Pieru, T., 2010. Petrography and major elements geochemistry of microgranular enclaves and Neoproterozoic granitoids of south Khasi, Meghalaya: Evidence of magma mixing and alkali diffusion during mingling of hybrid globules. J. Soc. India 76, 345–360.

Kumar, S., Pieru, T., Rino, V., Hayasaka, Y., 2017. Geochemistry and U-Pb SHRIMP zircon geochronology of microgranular enclaves and host granitoids from South Khasi Hills of the Meghalaya Plateau, NE India: evidence of synchronous mafic-felsic magma mixing-fractionation and diffusion in a post-collision tectonic environment during the Pan-African orogenic cycle. Geological Society of London, Special Publications, No. 457.

Kumar, S., Pieru, T., Rino, V., Lyngdo, B.C., 2005. Microgranular enclaves in Neoproterozoic granitoids of South Khasi hill, Meghalaya plateau, Northeast India: field evidence of interacting coeval mafic and felsic magmas. J. Geol. Soc. India 65, 629–633.

Kumar, S., Rino, V., 2006. Mineralogy and geochemistry of microgranular enclaves in Palaeoproterozoic Malanjkhand Granitoids, central India: evidence of magma mixing, mingling, and chemical equilibration. Contrib. Miner. Petrol. 152, 591–609.

Kumar, S., Rino, V., Pal, A.B., 2004. Field evidence of magma mixing from microgranular enclaves hosted in Early Proterozoic Malanjkhand granitoids, central India. Gondwana Res. 7, 539–548.

Kusky, T.M., Abdelsalam, M., Stern, R.J., Tucker, R.D., 2003. Preface: evolution of the East African and related orogens, and the assembly of Gondwana. Precambr. Res. 123, 81–85.

Labanieh, S., Chauvel, C., Germa, A., Quidelleur, X., 2012. Martinique: a clear case for sediment melting and slab dehydration as a function of distance to the trench. J. Petrol. 53, 2441–2464.

Langmuir, C.H., Vocke Jr., R.D., Gilbert, N.H., Stanley, R.H., 1978. A general mixing equation with applications to Icelandic basalts. Earth Planet. Sci. Lett. 37, 380–392.

Laurent, O., Zeh, A., Gerdes, A., Villaros, A., Gros, K., Słaby, E., 2017. How do granitoid magmas mix with each other? Insights from textures, trace element and Sr-Nd isotopic composition of apatite and titanite from the Matok pluton (South Africa). Contrib. Miner. Petrol. 172 (9), 80.

Leake, B.E., Woolley, A.R., Arps, C.E.S., Birch, W.D., Gilbert, M.C., Grice, J.D., Hawthorne, F.C., Kato, A., Kisch, H.J., Krivovichev, V.G., Linthout, K., Laird, J., Mandarino, J.A., Maresch, W.V., Nickel, E.H., Rock, N.M.S., Schumacher, J.C., Smith, D.C., Stephenson, N.C.N., Ungaretti, L., Whittaker, E.J.W., Youzhi, G., 1997. Nomenclature of amphiboles: report of the subcommittee on amphiboles of the international mineralogical association, Commission on new minerals and minerals name. Am. Mineral. 82, 1019–1037.

Lesher, C.E., 2010. Self-diffusion in silicate melts: theory, observations and applications to magmatic systems. Rev. Mineral. Geochem. 72, 269–309.

Liégeois, J.P., Stern, R., 2010. Sr-Nd isotopes and geochemistry of granite-gneiss complexes from the Meatiq and Hafafit domes, Eastern Desert, Egypt: no evidence for pre-Neoproterozoic crust. J. Afr. Earth Sc. 57 (1–2), 31–40.

Lofgren, G., 1974. An experimental study of plagioclase crystal morphology: isothermal crystallization. Am. J. Sci. 274, 243–273.

Mahdy, N.M., El Kalioubi, B.A., Wohlgemuth-Ueberwasser, C.C., Shalaby, M.H., El-Afandy, A.H., 2015. Petrogenesis of U- and Mo-bearing A2-type granite of the Gattar batholith in the Arabian Nubian Shield, Northeastern Desert, Egypt: Evidence for the favourability of host rocks for the origin of associated ore deposits. Ore Geol. Rev. 71, 57–81.

Monier, G., 1985. Cristallochimie des micas des leucogranites. Nouvelles données expérimentales et applications pétrologiques. Thèse d'État, Orléans, pp. 279.

Moussa, E.M.M., Stern, R.J., Manton, W.L., Ali, K.A., 2008. SIMS zircon dating and Sm/Nd isotopic investigations of Neoproterozoic granitoids, Eastern Desert, Egypt. Precambr. Res. 160, 341–356.

Nachit, H., Ibhi, A., Abia, E.H., Ohoud, M.B., 2005. Discrimination between primary magmatic biotites, reequilibrated biotites and neoformed biotites. C.R. Geosci. 337, 1415–1420.

Nelson, S.T., Montana, A., 1992. Sieve-textured plagioclase in volcanic rocks produced by rapid decompression. Am. Mineral. 77, 1242–1249.

O'Sullivan, G., Chew, D., Kenny, G., Henrichs, I., Mulligan, D., 2020. The trace element composition of apatite and its application to detrital provenance studies. Earth Sci. Rev. 201 (103044), 1–20.

Pascual, E., Donaire, T., Pin, C., 2008. The significance of microgranular enclaves in assessing the magmatic evolution of a high-level composite batholith: A case on the Los Pedroches Batholith, Iberian Massif, Spain. Geochem. J. 42, 177–198.

Paterson, S.R., Pignotta, G.S., Vernon, R.H., 2006. The Significance of microgranitoid enclave Shapes sand orientations. J. Struct. Geol. 26, 1465–1481.

Peccerillo, A., Taylor, A.R., 1976. Geochemistry of Eocene calc-alkaline volcanic rocks from the Kastamonu area, Northern Turkey. Contrib. Miner. Petrol. 58, 63–81.

Perugini, D., Poli, G., 2000. Chaotic dynamics and fractals in magmatic interaction processes: a different approach to the interpretation of mafic microgranular enclaves. Earth Planet. Sci. Lett. 175 (1), 93–103.

Perugini, D., Poli, G., Mazzuoli, R., 2003. Chaotic advection, fractals and diffusion during mixing of magmas: evidence from lava flows. J. Volcanol. Geoth. Res. 124 (3–4), 255–279.

Perugini, D., Ventura, G., Petrelli, M., Poli, G., 2004. Kinematic significance of morphological structures generated by mixing of magmas: a case study from Salina Island (southern Italy). Earth Planet. Sci. Lett. 222, 1051–1066.

Pesquera, A., Pons, J., 1989. Field evidence of magma mixing in the Aya granitic massif, (Basque Pyrenees, Spain). Neues Jahrbuch für Mineralogie Monatshefte 10, 441–454.

Poli, G., Tommasini, S., 1991. Origin and significance of microgranular inclusions in calc-alkaline granitoids: a proposed working model. J. Petrol. 32, 657–666.

Poli, G., Christofide, G., Koroneos, A., Trajanova, M., Zupančič, N., 2020. Multiple processes in the genesis of the Pohorje igneous complex: Evidence from petrology and geochemistry. Lithos 364–365, 105512.

Qian, Q., Hermann, J., 2013. Partial melting of lower crust at 10–15 kbar: constraints on adakite and TTG formation. Contribut. Mineral. Petrol. 165, 1195–1224.

Reid, J.B., Hamilton, M.A., 1987. Origin of Sierra Nevadan granite: Evidence from small scale composite dykes. Contrib. Miner. Petrol. 96, 441–454.

Renjith, M.L., Charan, S.N., Subbarao, D.V., Babu, E.V.S.S.K., Rajashekhar, V.B., 2013. Grain to outcrop-scale frozen moments of dynamic magma mixing in the syenite magma chamber, Yelagiri Alkaline Complex, South India. Geosci. Front. 5 (6), 801–820.

Richard, J.P., Uilrich, T., Kerrich, R., 2006. The Late Miocene-Quaternary Antofulla volcanic complex, southern Puna, NW Argentina: protracted history, diverse petrology, and economic potential. J. Volcanol. Geotherm. Resour. 152, 197–239.

Rodríguez, C., Castro, A., 2017. Silicic magma differentiation in ascent conduits. Experimental constraints. Lithos 272–273, 261–277.

Rodríguez, C., Castro, A., 2019. Origins of mafic microgranular enclaves and enclave swarms in granites: Field and geochemical relations. Geological Society of American Bulletin 131 (3–4), 635–660.

Sarjoughian, F., Azizi, M., Lentz, M.R., Ling, W., 2019. Geochemical and isotopic evidence for magma mixing/mingling in the Marshenan intrusion: Implications for juvenile crust in the Urumieh-Dokhtar Magmatic Arc, Central Iran. Geol. J. 54, 2241–2260.

Silva, M., Neiva, A., Whitehouse, M., 2000. Geochemistry of enclaves and host granites from the Nelas area, central Portugal. Lithos 50, 153–170.

Speer, J.A., 1984. Micas in igneous rocks. Mineralogical Society of America. Rev. Mineral. 13, 299–356.

Stein, M., Goldstein, S.L., 1996. From plume head to continental lithosphere in the Arabian- Nubian shield. Nature 382, 773–778.

Stern, R.J., Johnson, P., 2010. Continental lithosphere of the Arabian Plate: A geologic, petrologic, and geophysical synthesis. Earth-Sci. Rev. 101, 29–67.

Stern, R.J., 2002. Crustal evolution in the East African Orogen: a neodymium isotopic perspective. J. Afr. Earth Sc. 34, 109–117.

Stern, R.J., 2018. Neoproterozoic formation and evolution of Eastern Desert continental crust-the importance of the infrastructure-superstructure transition. J. Afr. Earth Sci. 146, 15–27.

Stern, R.J., Avigad, D., Miller, N.R., Beyth, M., 2006. Evidence for the Snowball Earth hypothesis in the Arabian-Nubian Shield and the East African Orogen. J. Afr. Earth Sci. 44, 1–20.

Stern, R.J., Gottfried, D., Hedge, C.E., 1984. Late Precambrian rifting and crustal evolution in the northeastern Desert of Egypt. Geology 12, 168–172.

Stern, R.J., Hedge, C.E., 1985. Geochronological and isotopic constraints on the Late Precambrian crustal evolution in the Eastern Desert of Egypt. Am. J. Sci. 285, 97–127.

Stoeser, D.W., Frost, C.D., 2006. Nd, Pb, Sr and O isotope characterization of Saudi Arabian Shield terranes. Chem. Geol. 226, 163–188.

Streckeisen, A., Le Maitre, R.W., 1979. A chemical approximation to the modal QAPF classification of the igneous rocks. Egypt. Neues Jahrbuch für Mineralogie - Abhandlungen: J. Mineral. Geochem. 136, 169–206.

Sun, S.S., McDonough, W.F., 1989. Chemical and isotopic systematics of oceanic basalts: implications for mantle composition and processes. In: Saunders, A.D., Norry, M.J. (Eds.), Magmatism in the Ocean Basins, 42. Geological Society of London Special Publication, pp. 313–345.

Tatsumi, Y., 2000. Continental crust formation by crustal delamination in subduction zones and complementary accumulation of the enriched mantle I component in the mantle. Geochem. Geophys. Geosyst. 1 (12).

Taylor, S.R., Mclennan, S.M., 1985. The Continental Crust: Its Composition and Evolution; An Examination of the Geochemical Record Preserved in Sedimentary. RocksBlackwell, Oxford, p. 312.

Taylor, S.R., McLennan, S.M., 1995. The geochemical evolution of the continental crust. Rev. Geophys. 33, 241–265.

Tischendorf, G., Gottesmann, B., Förster, H.-J., Trumbull, R.B., 1997. On Li-bearing micas: estimating Li from electronmicroprobe analyses and an improved diagram for graphical representation. Mineral. Mag. 61, 809–834.

Turner, S., Foden, J., 2001. U, Th and Ra disequilibria, Sr, Nd and Pb isotope and trace element variations in Sunda arc lavas: predominance of a subducted sediment component. Contrib. Mineral. Petrol. 142, 43–57.

Vernon, R.H., 1983. Restite, xenoliths and microgranitoid enclaves in granites. J. Proceed. Roy. Soc. New South Wales 116, 77–103.

Vernon, R.H., 1984. Microgranitoid enclaves in granites - globules of hybrid magma quenched in a plutonic environment. Nature 309, 438–439.

Vernon, R.H., 1990. Crystallization and hybridism in microgranitoid enclave magmas: microstructural evidence. J. Geophys. Res. 95, 17849–17859.

Vernon, R.H., 1991. Interpretation of Microstructures of Microgranitoid Enclaves. In: Didier, J., Barbarin, B. (Eds.), Enclaves and Granite Petrology 13. Elsevier, Amsterdam, pp. 277–292.

Vernon, R.H., Etheridge, M.A., Wall, V.J., 1988. Shape and microstructure of microgranitoid enclaves: Indicators of magma mingling and flows. Lithos 22, 1–11.

Watson, E.B., Jurewicz, S.R., 1984. Behaviour of alkalis during diffusive interaction of granitic xenoliths with basaltic magma. J. Geol. 92, 121–131.

Weinberg, R.F., Sial, A.N., Pessoa, R.R., 2001. Magma flow within the Tavares pluton, northeastern Brazil: Compositional and thermal convection. Geol. Soc. Am. Bull. 113, 508–520.

White, A.J.R., Chappell, B.W., Wyborn, D., 1999. Application of the restite model to the Deddick Granodiorite and its enclaves: a reinterpretation of the observations and data of Maas et al. (1998). J. Petrol. 40, 413-421.

Wilson, M., 1989. Igneous Petrogenesis, a Global Tectonic Approach. Unwin Hyman, p. 466.

Xiao, Y., Chen, S., Niu, Y., Wang, X., Xue, Q., Wang, G., 2020. Mineral compositions of syn-collisional granitoids and their implications for formation of juvenile continental crust and adakitic magmatism. J. Petrol. 61, 1–19.

Zafar, T., Rehman, H.U., Mahar, M.A., Alam, M., Oyebamiji, A., Rehman, S.U., Leng, C. B., 2020. A critical review on petrogenetic, metallogenic and geodynamic implications of granitic rocks exposed in north and east China: New insights from apatite geochemistry. J. Geodyn. 136, 101723.

Zhang, J., Wang, T., Castro, A., Zhang, L., Shi, X., Tong, Y., Zhang, Z., Guo, L., Yang, Q., Iaccheri, L.M., 2016. Multiple Mixing and Hybridization from Magma Source to Final Emplacement in the Permian Yamatu Pluton, the Northern Alxa Block, China. J. Petrol. 57 (5), 933–980.

Zhou, X.R., 1994. Hybridization in the genesis of granitoids. Earth Sci. Front. 1 (1–2), 87–97.

Zhou, Z.X., 1986. The origin of intrusive mass in Fengshandong, Hubei Province. Acta Petrol. Sin. 29 (1), 59–70.

Zhu, J., Wang, R., Zhang, P., Xie, C., Zhang, W., Zhao, K., Xie, L., Yang, C., Che, X., Yu, A., Wang, L., 2009. Zircon U-Pb geochronological framework of Qitianling granite batholith, middle part of Nanling Range, South China. Sci. China, Ser. D Earth Sci. 52 (9), 1279–1294.

Zorpi, M., Coulon, C., Orsini, J., Cocirta, C., 1989. Magma mingling, zoning and emplacement in calc-alkaline granitoid plutons. Tectonophysics 157, 315–329.